https://doi.org/10.5194/soil-2021-55
Preprint. Discussion started: 24 August 2021

Potential and limits of vegetation indices compared to evaporite mineral indices for soil salinity discrimination and mapping

Abderrazak Bannari [1] and Abdelgader Abuelgasim [2]

[1] Space Pix-Map International Inc., Gatineau (Québec) J8R-3R7, Canada. Email: abannari@bell.net

[2] Department of Geography and Urban Sustainability, United Arab Emirates University, AL-Ain 15551, United Arab Emirates. Email: a.abuelgasim@uaeu.ac.ae

Correspondence to: abannari@bell.net

Abstract. The study aims to analyze the ability of the most popular and widely used vegetation indices (VI's), including NDVI, SAVI, EVI and TDVI, to discriminate and map soil salt contents compared to the potential of evaporite mineral indices such as SSSI and NDGI. The proposed methodology leverages on two complementary parts exploiting simulated and imagery data acquired over two study areas, i.e. Kuwait-State and Omongwa salt-pan in Namibia. In the first part, a field survey was conducted on the Kuwait site and 100 soil samples with various salinity levels and contents were collected; as well as, herbaceous vegetation cover canopy (alfalfa and forage plants) with various LAI coverage rates. In a Goniometric-Laboratory, the spectral signatures of all samples were measured and transformed using the continuum removed reflectance spectrum (CRRS) approach. Subsequently, they were resampled and convolved in the solar-reflective spectral bands of Landsat-OLI, and converted to the considered indices. Meanwhile, soil laboratory analyses were accomplished to measure pHs, electrical conductivity (EC_{-Lab}), the major soluble cations and anions; thereby the sodium adsorption ratio was calculated. These elements support the investigation of the relationship between the spectral signature of each soil sample and its salt content. Furthermore, on the Omongwa salt-pan site, a Landsat-OLI image was acquired, pre-processed and converted to the investigated indices. Mineralogical ground-truth information collected during previous field work and an accurate Lidar DEM were used for the characterization and validation procedures on this second site. The obtained results demonstrated that regardless of the data source (simulation or image), the study site and the applied analysis methods, it is impossible for VI's to discriminate or to predict soil salinity. In fact, the spectral analysis revealed strong confusion between signals resulting from salt-crust and soil optical properties in the VNIR wavebands. The CRRS transformation highlighted the complete absence of salt absorption features in the blue, red and NIR wavelengths. As well as the analysis in 2D spectral-space pointed-out how VI's compress and completely remove the signal fraction emitted by the soil background. Moreover, statistical regressions ($p < 0.05$) between VI's and EC_{-Lab} showed insignificant fits for SAVI, EVI and TDVI ($R^2 \leq 0.06$), and for NDVI (R^2 of 0.35). Although the Omongwa is a natural flat salt playa, the four derived VI's from OLI image are completely unable to detect the slightest grain of salt in the soil. Contrariwise, analyses of spectral signatures and CRRS highlighted the potential of the SWIR spectral domain to distinguish salt content in soil regardless of its optical properties. Likewise, according to Kuwait spectral data and EC_{-Lab} analysis, NDGI and SSSI incorporating SWIR wavebands have performed very well and similarly (R^2 of 0.72) for the differentiation of salt-affected soil classes. These statistical results were also corroborated visually by the maps derived from these evaporite indices over the salt-pan site, as well as by their

https://doi.org/10.5194/soil-2021-55
Preprint. Discussion started: 24 August 2021

consistency with the validation points representing the ground truth. However, although both the indices have mapped the salinity patterns almost similarly, NDGI further highlights the gypsum content. While the SSSI show greater sensitivity to salt crusts present in the pan area that are formed from different mineral sources (i.e., halite, gypsum, etc.).

1. Introduction

Soil salinity or salinization is a global environmental threat, it occurs in different geographical zones characterized by different climatic conditions and can result from both natural and anthropogenic actions (Shahid et al., 2018). In humid zones, rainfalls exceeds the evaporation, thus the soluble salts are leached from the soil surface to deeper zone. While, semi-arid and arid lowlands are more affected because of near surface saline groundwater and due to evaporation exceeding precipitations (Dehaan and Taylor, 2002; Shahid and Rahman, 2011). Moreover, soil salinity is associated with several other physical factors including soil properties, permeability, geomorphology, geology, micro-topography, wastewater use and climate variability (Hartemink, 2014; Shahid and Behnassi, 2014; Dagar et al., 2016; Bannari and Al-Ali, 2020; Bannari et al., 2021). During the past decades the global warming has decreased precipitations, increased temperatures, reduced soil moisture regime and, subsequently, accelerated expansion of this menacing phenomenon. Indeed, it represents a serious problem for health and functionality of arid ecosystems, significant impacts on land desertification, reduction of crop production and economic aspects (Mougenot et al., 1993; Naing'OO et al., 2013; Arrouays et al., 2017; FAO, 2018; Ivushkin et al., 2019; Hassani et al., 2020); as well as on human wellbeing and sustainable development. Whereas, in irrigated agricultural lands, salinity occurs when salts are concentrated in soils by the evaporation of irrigation water. The major causes are a combination of poor land management and crude irrigation practices, which cause changes in soil and vegetation cover, and ultimately loss of vegetation and agricultural productivity (Metternicht and Zinck, 2003; Masoud and Koike, 2006; Corwin and Scudiero, 2019; Zhu et al., 2021; Gopalakrishnan and Kumar, 2021). Obviously, combating soil salinization should lead to enhance soil fertility, agricultural productivity and profitability, and ensure food security (Teh and Koh, 2016).

Furthermore, it is common that both saline and sodic conditions occur together in the soil. Salinity refers to the amount of soluble salts in soil, such as sulfates (SO_4), carbonates (CO_3), and chlorides (Cl^-) mainly of sodium (Na), Calcium (Ca), Potassium (K), Magnesium (Mg) and other cations to a lesser extent (Richards, 1954). The solubility of halite (NaCl), calcium sulphate-anhydrite ($CaSO_4$) and gypsum ($CaSO_4.2H_2O$) is used as a standard for comparing the levels of salinity content in the soil. According to Richards (1954), a soil is said to be saline when it has an electrical conductivity of saturation extract (ECe) greater than 4 $dS.m^{-1}$ at 25°C and a pHs < 8.2. While sodicity refers to the exchangeable sodium (Na^+) relative to exchangeable Ca^{2+} and Mg^{2+} in soil. Sodicity has a strong influence on the soil structure, dispersion occurs when the clay particles swell strongly and separate from each other on wetting. On drying, the soil becomes dense, cloddy, and without structure (Charters, 1993; Sumner et al. 1998). Sodic soils have a pHs greater than 8.2 and a preponderance of sodium, carbonate and bicarbonate (Richards 1954). Ranges of salinity are usually described as non-saline, very slightly saline, slightly saline, moderately saline, and strongly saline (high to extreme) based on the ECe values (USDA, 2014; Metternicht and

https://doi.org/10.5194/soil-2021-55
Preprint. Discussion started: 24 August 2021

Zinck, 1997; Soil Science Division Staff, 2017). Traditionally, soil salinity is measured by geophysical method (EM38) in the field (apparent salinity) and through laboratory determination (EC_{-Lab}) using water extracted from a saturated soil paste which is globally accepted a standard to quantify soil salinity (Norman, 1989; USDA, 2004 and 2014; Zhang et al., 2005). Unfortunately, the laboratory method is expensive, time-consuming, and laborious when large area is to be investigated, especially for temporal salinity monitoring. Thus, remote sensing science, technology and image processing methods have outperformed ground-based methods, and they have been used for identifying, mapping and monitoring salt-affected zones (Masoud and Koike, 2006; Meternich and Zinck, 2009; Ben-Dor et al., 2009; Nawar et al., 2014; Wu et al., 2014; El-Battay et al., 2017; Bannari et al., 2018 and 2020; Bannari, 2019; Davis et al., 2019; Al-Ali et al., 2021).

Previously, photo-interpretation approaches have been adopted to follow the development and the dynamics of soil salinity and sodicity in space and time (Manchanda and Khanna, 1979; Rao et al., 1991). These approaches have been based on the analysis of colour-infrared photographs or on the false color composites of images acquired from space with the first generation of Landsat sensors (MSS and TM). Nevertheless, the advancements in multispectral, hyperspectral, thermal, and radar technologies with significant radiometric performances and high signal-to-noise ratio (SNR) are providing the best and the newest opportunities for more precise and more effective salinization detection and prediction (Dehaan and Taylor, 2002; Metternicht and Zinck, 2003; Lasne et al., 2009; Fan et al., 2016; Nurmemet et al., 2018; Abuelgasim et al., 2018; Hoa et al., 2019; Wang et al., 2020). Indeed, thanks to the free availability of remote sensing data acquired with different sensors onboard various platforms, soil salinity was modeled for global, regional and local scales using, respectively, coarse, moderate and high spatial resolutions, i.e., MODIS, Landsat, Sentinel, Ikonos, and Worldview (Shamsi et al., 2013; Alexakis et al., 2016; Bannari et al., 2017a; Kasim et al., 2018; Whitney et al., 2018; Ivushkin et al., 2019; Bannari, 2019; Moussa et al., 2020; Hassani et al., 2020; Al-Ali et al., 2021). However, the most frequently used data to investigate and map soil salinity remain those acquired by remote sensing sensors with medium spatial and spectral resolutions, such as Landsat series (TM, ETM+, and OLI) and Sentinel-MSI (Joshi et al., 2002; Metternicht and Zinck, 2009; Fan et al., 2016; El-Battay et al., 2017; Bannari et al., 2018 and 2020; Davis et al., 2019; Taghadosi et al., 2019; Wang et al., 2019).

Otherwise, in addition to remote sensing sensors technologies improvement and innovation, numerous image processing approaches and models were also developed and applied for soil salinity retrieval. They include mixture-tuned matched filter approach (Dehaan and Taylor, 2003), regression of multi-spectral bands (Lobell et al., 2010; Fan et al., 2012; Sidike et al., 2014), partial least square regression (Fan et al., 2015; Wang et al., 2018; Gopalakrishnan and Kumar, 2020), multivariate adaptive regression splines (Nawar et al., 2015), artificial neural network model (Farifteh et al., 2008; Jiang et al., 2019; Boudibi et al., 2021), linear spectral mixture analysis (Ghosh et al., 2012; Masoud et al., 2019), spectral angle mapper (Bharti et al., 2015; Wang et al., 2021), support vector machines (Gleeson et al., 2010; Jiang et al., 2019), and machine learning regression (Wu et al., 2018; Hassani et al., 2020). Definitely, these sophisticated and complicated methods require extensive training information and/or ground endmembers measurements. However, the simplicity of empirical and/or semi-empirical methods based on spectral indices are easier to transfer between sensors and can be used as a robust alternative compared to the revolutionary and complex modelling methods; because they are based on the knowledge of spectral absorption features that

https://doi.org/10.5194/soil-2021-55
Preprint. Discussion started: 24 August 2021

characterize specifically the target under investigation (Rouse et al., 1974; Peon et al., 2017, Milewski et al., 2019). Moreover, they have the advantage of being reproducible, easily transferable and applicable in other geographic regions (Mulder et al., 2011).

In the literature, some evaporite mineral indices have been proposed for soil salinity detection and mapping. For instance in Pakistan, Khan et al. (2001) proposed three soil salinity indices based on red and near-infrared (NIR) bands of LISS-II sensor onboard the Indian satellite IRS-1B. These indices are named Brightness Index (BI), Normalized Difference Salinity Index (NDSI) and Salinity Index (SI). Among them, the authors found that the NDSI is the most promising for different salinity classes' characterization in semi-arid environment using satellite images and *in situ* observations. In irrigated agricultural land in Syria, Al-Khaier (2003) highlighted the importance of shortwave infrared (SWIR) bands of Landsat-ETM+ and ASTER for soil salinity contents discrimination. He proposed the Salinity Index ($SI_{\text{-ASTER-4,5}}$) based on bands 4 and 5 of ASTER sensor (i.e., B4: 1.6-1.7 µm and B5:2.145-2.185 µm) or the bands 5 (SWIR-1) and 7 (SWIR-2) of Landsat-ETM+. Based on the field soil sampling and $EC_{\text{-Lab}}$, the validation of this index showed a very good potential for salt-affected soil prediction. Moreover, in the context of a cooperative project between India and the Netherlands (IDNP, 2002) three soil salinity indices were proposed. These indices integrate the NIR and SWIR bands of Landsat-TM, and are named SI-1, SI-2 and SI-3. Combining field soil survey, soil chemical laboratory analysis, spectroscopy measurements and ALI-EO-1 image, Bannari et al. (2008a and 2016) demonstrated that the SWIR bands are more sensitive than other bandwidths to discriminate among different soil salinity classes, particularly slight and moderate salinity in irrigated agricultural lands. Consequently, they proposed the Soil Salinity and Sodicity Index (SSSI) integrating the SWIR bands of ALI-EO or Landsat-OLI sensors. Recently, based on the gypsum absorption feature in 1.75 µm and following the same concept behind the development of normalized difference vegetation index (NDVI), Milewski et al. (2019) proposed the normalized difference gypsum index (NDGI). This new index exploits the most relevant narrow wavelengths characterizing the gypsum absorption features: 1690 and 1750 µm. It has been tested on Omongwa salt-pan area in Namibia, which is a natural flat salt playa dominated by evaporite minerals such as halite, gypsum, calcium carbonate, and minor content of clay (Mees, 1999; Fookes and Lee, 2018; Genderjahn et al., 2018). Using hyperspectral data acquired with diver sensors (space-borne Hyperion, airborne HySpex, and simulated space-borne EnMAP imagery), spectroradiometric measurements, XRD mineralogical analyses; as well as, applying continuum removed reflectance spectrum (CRRS), slop and half-area processing methods, the validation of NDGI provides satisfactory results (Milewski et al., 2019). Coincidentally, the NDGI is simply the $SI_{\text{-ASTER-4,5}}$ proposed 16 years ago by Al-Khaier (2003). Otherwise, we end up with the same index under two different names and different authors, particularly when the SWIR bands of Landsat sensors or Sentinel-MSI are used, as well as the bands 4 and 5 of ASTER. Obviously, the difference between them is clear when using hyperspectral data.

In other respects, since the emergence of remote sensing as a new scientific discipline in the early 1970s, vegetation indices (VI's) were involved as radiometric measurements of the spatial and temporal distribution of vegetation photo-synthetically active. Based on the strong chlorophyll absorption in red and intense reflectivity by the canopy biomass in NIR, these indices play an important role in deriving various biophysical and physiological parameters, including percentage of vegetation cover, leaf area index (LAI), absorbed photo-synthetically active radiation (APAR), production rate of the biomass, etc. Moreover, their interest lies in the detection of changes in land use and the monitoring of the seasonal dynamics of vegetation on local, regional and global scales (Leeuwen et al., 1999). Based on the red and NIR bands, the NDVI was proposed by Rouse et al. (1974) at the dawn of remote sensing. Since these two spectral bands are generally present on Earth observation and meteorological satellites, and often contain more than 90% of the information relating to vegetation canopy (Baret, 1986; Bannari et al., 1995), the NDVI had taken a privileged place in the NASA/NOAA Pathfinder project (James and Kalluri, 1994). Thus, it was daily derived from NOAA-AVHRR data at the Earth scale. Subsequently, it was also derived every day from MODIS and SPOT-Vegetation data to produce a time series products for global vegetation assessment and monitoring at the regional and global scales (Chéret and Denux, 2011; Hameid and Bannari, 2016; Liu et al., 2021). Due to this glorious history and its simplicity, the NDVI has become the most widely used to assess vegetation. However, despite its popularity and its capability to reduce the sun illumination geometry and to normalize the topographic variations (Kaufman and Holben, 1993; Bannari et al., 1995), the NDVI shows some sensitivity to the atmosphere (scattering and absorption) and soil background artefacts (color, brightness, texture, etc.). To overcome these limitations, more than fifty VI's have been developed and proposed for various applications and under specific conditions (Bannari et al., 1995). However, despite these new development and innovative efforts, the use of VI's to characterize vegetation canopy remains limited by various physical factors that affect the recorded signal at the satellite level, such as atmosphere, sensor-drift, topography, soil background optical properties, saturation, linearity, and BRDF (Price, 1987; Myneni and Asrar, 1994; Running et al., 1994; Burgess et al., 1995; Bannari et al., 1996; Teillet et al., 1997; Huete et al., 1997; Bannari et al., 1999).

Cert, the majority of these limiting factors can be corrected on remote sensing imagery or *in situ* measurements before the extraction of such index; except the impact of the optical properties of the soil background. This last factor has been considered in the theoretical concept supporting many VI's development for minimising or removing completely the contribution of the soil underlying the canopy on the remotely sensed signal and, therefore, to enhance that resulting from the biomass. For instance, the soil adjusted vegetation index **(**SAVI) was proposed by Huete (1988) to minimize the artefacts caused by soil background on the estimation of vegetation cover fraction by incorporating a correction factor "L". Moreover, to overcome the limitations of linearity and saturation, to reduce the noise of atmospheric effects, and to remove the artefacts of soil optical properties, the enhanced vegetation index (EVI) was proposed also by Huete *et al.* (2002). Furthermore, the transformed difference vegetation index (TDVI) was proposed by Bannari *et al.* (2002) to describe the vegetation cover fraction independently to the soil-background, to reduce the saturation problem, and to enhance the vegetation dynamic range linearly. These indices (NDVI, SAVI, EVI, and TDVI) were developed and used to establish a close relationship between radiometric responses and vegetative cover densities. However, despite their particular mission of assessing and managing vegetation covers, many users of remote sensing applied these indices for soil salinity detection and mapping (Fernandez-Buces et al., 2006; Aldakheel, 2011; Allbed et al., 2014; Asfaw et al., 2016; Elhag, 2016; Azabdaftari and Suna, 2016; Ferdous and Rahman, 2017; Neto et al., 2017; Peng et al., 2019; Taghadosi et al., 2019**;** Nguyen et al., 2020; Zhu et al., 2021; Golabkesh et al., 2021). Hence the interest of this research to investigate what VI's can really tell us about the discrimination of soil salinity classes'. The most popular and widely used indices presented

https://doi.org/10.5194/soil-2021-55
Preprint. Discussion started: 24 August 2021

above (NDVI, SAVI, EVI and TDVI) are considered and compared to the newly proposed evaporite mineral indices (NDGI and SSSI). In this regard, a field survey was conducted for soil and vegetation cover sampling, soil laboratory analysis, spectral measurements in a Goniometric-Laboratory, and Landsat-OLI image were used. Two study-sites in arid environments are considered, the Kuwait-State in the Middle-East desert and the Omongwa salt-pan located in the southwest of Kalahari desert in Namibia.

2. Materials and Methods

Fig. 1 summarizes the applied methodology by combining two independent datasets (simulated and image) acquired over two different study areas located in Kuwait and Namibia. On the Kuwait site, a field survey was conducted and 100 soil samples were collected with various salt contents; as well as a vegetation cover was sampled at different LAI coverage rates. Then, the bidirectional reflectance factor was measured above each sample of soil and vegetation in a Goniometric-Laboratory using an Analytical Spectral Device (ASD) spectroradiometer (ASD, 2015). After the spectral measurements, laboratory analyses of soil samples were achieved to measure the water soluble cations (Ca^{2+}, Mg^{2+}, Na^{+}, and K^{+}) and anions (Cl^{-} and SO_4^{2-}) in the extract from saturated soil paste, the pH of saturated soil paste (pHs) and the electrical conductivity (EC_{-Lab}) of the extract from saturated soil paste; as well as the sodium adsorption ratio (SAR) being calculated using standard calculation procedure (USDA, 2004 and 2014; Zhang et al., 2005). The results of these analyses provided reliable information on the type and degree of salinity and sodicity in each soil sample. Thus, they support the interpretation of the complex and close relationship between the soil-salt contents and their spectroradiometric behaviours. Furthermore, the measured spectra of the most representative soil salinity classes and LAI densities were transformed using the CRRS (Clark et al., 1987). Likewise, all measured spectra were resampled and convolved in the solar-reflective spectral bands of OLI sensor using the Canadian Modified Simulation of a Satellite Signal in the Solar Spectrum (CAM5S) radiative transfer code (Teillet and Santer, 1991), and the relative spectral response profiles characterizing the OLI sensor filters of each spectral band. Afterwards, the considered indices were calculated and analysed spectrally, as well as fitted statistically with EC_{-Lab}. While, on the Omongwa salt pan site, the acquired OLI image was pre-processed and converted to the investigated indices. Published by Milewski et al. (2017), mineralogical ground-truth information collected during previous field work and analysed in the laboratory, and an accurate Lidar DEM were used for the characterization and validation of the results obtained on this second site.

[Figure 1]

2.1. **Study areas**

The state of Kuwait (Fig. 2) situated in the north western part of the Arabian Peninsula (29.40^0 N and 47.50^0 E) is characterized by an arid climate, very hot summers (47 °C) and irregular precipitations with an annual mean of 118 mm. The main geomorphological features characterized the study area are escarpments, sand dunes, Sabkhas (pure salt accumulation), depressions, playas and alluvial fans (Al-Sarawi, 1995). These features are controlled by three types of surface deposits. The first is represented by Aeolian deposits such as dunes and sand sheet. The second is identified by evaporites including sodium chloride (halite, NaCl), calcium carbonate (calcite, $CaCO_3$), gypsum

https://doi.org/10.5194/soil-2021-55
Preprint. Discussion started: 24 August 2021

($CaSO_4.2H_2O$), and anhydrite ($CaSO_4$) in coastal and inland Sabkhas. The third include fluvial deposits such as pebbles and gravels, which are located along the Wadis channels. Each of these deposits has specific geomorphic characteristics based on their origin, topography that is generally flat with low relief, and climatic impacts. Geologically, Kuwait stratigraphy consists of two stratigraphic groups; Kuwait Group and Hasa Group (Milton, 1967) consisting of six Formations, four of them are exposed in the outcrops represented by Dammam, Ghar, Mutla and Jal-AzZor Formations. In Hassa Group, the Dammam Formation *(Eocene)* consists of white fine grained cherty limestone and forms some karst; however, the three other Formations are composed mostly of sandy limestone, calcareous sandstones, sand and clay. Soils of Kuwait are mostly categorized as sandy with limited organic matter, very low nutrient and very high amount of calcareous materials. Moreover, Gatch layer occurs in many Kuwaiti soils, which is considered a calcic and/or gypsic pan (Milton, 1967).

[Figure 2]

The Omongwa salt-pan area is a natural flat salt playa covering approximately 20 km^2 (Fig. 3), located in the south-west of Kalahari region in Namibia (23°43'S and 19°22'E) at 1200 m altitude above sea level (Genderjahn et al., 2018). The climate is arid and hot, the average annual temperature is about 20°C with a maximum around 48°C during the summer (July and August), the average precipitation is about 220 mm/year, and the evaporation exceeds precipitations. This area is devoid of vegetation except some scattered halophytes in the peripheral neighbourhood of the north-western of the playa (Milewski et al., 2017). The pan soils are characterized by very low organic matter content and mixed evaporite sediments (photos in Fig. 3) including halite, gypsum, calcium carbonate, and minor content of clay (Mees, 1999; Fookes and Lee, 2018; Genderjahn et al., 2018). However, the upper soil surfaces are mostly dominated by halite crust in variable quantities (Bryant, 1996; Lowenstein and Hardie, 1985), which is formed over time due to the succession of flooding events in the winter and high temperatures during the summer, as well as the contribution of wind activity (Schuller et al., 2018; Milewski et al., 2017).

[Figure 3]

2.1. Soil and vegetation cover sampling

Soils of Kuwait are mostly sandy with a very low organic matter and are infertile (USDA, 1999). They have been classified into two main soil orders; the Aridisols occupying 70.8% and the Entisols occupying 23.2% of the area surveyed, while the other restricted and marginal groups are representing the remaining percentage (6.64%). These two soil orders are further classified into eight soil great groups based on morphological, mineralogical, chemical and physical characteristics (Omar and Shahid, 2013; USDA, 1999). The extreme soil salinity class (Sabkhas) occurs in the Aquisalids soil great group on coastal flats and inland Playas, which contain very high salt contents and gypsum. High soil salinity class is identified in Haplocalcids that attribute to layer of carbonate masses and salt contents. Moderate to low salinity class occurs in Petrocalcids soil, which is characterised by calcic hardpan overlying sandy to loamy soils and presence of scattering halophytes.

https://doi.org/10.5194/soil-2021-55
Preprint. Discussion started: 24 August 2021

Field survey was organized in the center and the east of Kuwait territory (Fig. 2), it includes irrigated agricultural fields, desert land, urban areas, coastal zones, and low-land such as Bubiyan Island. Based on the fieldwork and soil map, the following soil salinity classes represented by photos in Fig. 2 were considered: non-saline (A), low (B), moderate (C), high (D), very high, and extreme salinity (F). The field survey was organized during four days (15^{th} to 18^{th} May 2017), and geo-referenced 100 soil samples representing these classes were collected from upper layer of the soil (0 to 5 cm deep considering an area about 50 × 50 cm), placed and numbered in plastic bags. In addition, each soil sample was physically described (color, brightness, texture, etc.), photographed, and geographically localized using accurate GPS ($\sigma \leq \pm$ 30 cm).

Furthermore, at a medium growth stage, herbaceous vegetation cover canopy (alfalfa and forage plants) with different LAI coverage rates were collected from the cultivated agricultural fields. A sampling quadrate of 50 cm by 50 cm was used, and all the aboveground biomass (approximately 70 cm height) was harvested within this area. The samples were immediately stored in bags in a cooler and transported to the laboratory for spectroradiometric measurements as discussed in the following section 2.3.

2.2. Soil laboratory analysis

In the laboratory, the considered soil samples were air-dried, ground, and passed through 2 mm sieve. After the spectral signatures measurements, the saturated soil paste extract method was utilized to measure the EC_{-Lab} and pH of saturated soil paste (pHs). Moreover, the major soluble cations (Ca^{2+}, Mg^{2+}, Na^{+}, and K^{+}) and anions (Cl^{-} and SO_4^{2-}) were measured, and the sodium adsorption ratio (SAR) was calculated. These analyses have been carried out at the soil laboratory using methods that meet the current international standards in soil science (Richards, 1954; Zhang et al., 2005; USDA, 2004 and 2014).

2.3. Spectroradiometric measurements

Spectroradiometric measurements were acquired in the Goniometric-Laboratory using an ASD (*Analytical Spectral Devices* Inc., Longmont, CO, USA) FieldSpec-4 Hi-Res (high-resolution) spectroradiometer (ASD, 2015). Equipped with two detectors with hyperspectral resolution covering the VNIR and SWIR wavelengths (350 and 2500 nm), the ASD measures a continuous spectrum with a 1.4 nm sampling interval from 350 to 1000 nm and a 2 nm from 1000 to 2500 nm; then it resamples the measurements in 1-nm intervals allowing the acquisition of 2151 contiguous bands per spectrum. The sensor is characterized by the programming capacity of the integration time, which allows an increase of the SNR as well as stability.

The bidirectional reflectance spectra were measured above each air-dry soil sample at nadir with a field of view (FOV) of 25° and a solar (Halogen floodlights) zenith angle of approximately 5° by averaging forty measurements. The ASD was installed at a height of 60 cm approximately over the target, which makes it possible to observe a surface of approximately 700 cm^2. Each soil sample was placed on a black surface to minimise the multiple scattering effects allowing only the observation and the measurements of the soil signal. For vegetation cover, the plants were fixed vertically in a black wooden box filled with soil to imitate the *in-situ* canopy at different LAI coverage's. Similarly to soil samples, the box was placed on a large black surface to minimise the multiple

https://doi.org/10.5194/soil-2021-55
Preprint. Discussion started: 24 August 2021

scattering impacts and only measure the signal reflected by the vegetation canopy. While at this time, the height of the ASD was about 100 cm over the canopy allowing the observation of a surface with a diameter of 44 cm. A laser beam was used to locate the center of the ASD-FOV over the center of each target. The reflectance factor of each sample (soil or vegetation) was calculated by rationing target radiance to the radiance obtained from a calibrated "Spectralon panel" (Labsphere, 2001) in accordance with the method described by Jackson *et al.* (1980). Moreover, the corrections were applied for the wavelength dependence and non-lambertian behaviour of the panel (Sandmeier et al., 1998; ASD, 2015; Ben-Dor et al., 2015).

[Figure 4]

2.4. Continuum-removal

Spectral signatures are processed and transformed using numerous approaches to retrieve information regarding the change in reflectance of particular target over a specific bandwidth between 350 and 2500 nm (Van-Der-Meera, 2004). For instance, absorption features (position, depth, width, and asymmetry) are used to quantitatively estimate the mineral or chemical composition of samples from the measured spectra in the field, in the laboratory and/or from hyperspectral images. To emphasize these absorption features, many approaches were proposed including relative absorption-band-depth (Crowley et al., 1989), spectral feature fitting technique, and Tricorder and Tetracorder algorithms (Clark et al., 2003). These approaches work on so-called CRRS approach, thus recognizing that the absorption in a spectrum has a continuum and individual absorption features (Clark *et al.*, 1987; Van-Der-Meera, 2004; Clark *et al.*, 2014). Proposed by Clark and Roush (1984), CRRS transformation and analysis allows the isolation of individual absorption features in the hyperspectral signature of a specific target under investigation, analysis and comparison. It normalizes the original spectra and helps to compare individual absorption features from a common baseline (Clark *et al.*, 1987). The continuum is a convex hull fit over the top of a spectrum under study using straight-line segments that connect local spectra maxima. The first and last spectral data values are on the hull; therefore, the first and last bands in the output continuum-removed data file are equal to 1.0. In other words, after continuum removed, a part of the spectrum without absorption features will have a value of 1, whereas complete absorption would be near to 0, with most absorptions falling somewhere in between. The CRRS approach was used for discriminating and mapping rocks and minerals (Clark et al., 1990; Clark and Swayze, 1995), soil salinity (Farifteh, 2007; Nawar et al., 2014; Bannari et al., 2018; Mousa et al., 2019; Milewski et al., 2019), as well as vegetation cover (Kokaly et al., 2003; Huang et al., 2004; Manevski et al., 2011). In this study, the continuum algorithm implemented in ENVI image processing system was used (ENVI, 2012).

2.5. Spectral sampling and convolving in Landsat-OLI bands

As discussed above, the measured bidirectional reflectance factors with the ASD have a 1-nm interval allowing the acquisition of 2151 contiguous hyperspectral bands per spectrum. However, most multispectral remote sensing sensors measure the reflectance that is integrated over broad bands. Consequently, the measured spectra of each soil and each vegetation sample was resampled and convolved to match the solar-reflective spectral responses functions

https://doi.org/10.5194/soil-2021-55
Preprint. Discussion started: 24 August 2021

characterizing the optics and electronics of OLI instrument in the VNIR and SWIR spectral bands. In this step, the resampling procedure considers the nominal width of each spectral band. Then, the convolution process was executed using the CAM5S radiative transfer code (RTC). This fundamental step simulates the signal received by OLI sensor at the top of the atmosphere from a surface reflecting solar and sky irradiance at sea level, considering the filter of each individual band, and assuming ideal atmospheric conditions without scattering or absorption (Steven et al., 2003; Zhang and Roy, 2016). The reflectance values of soil samples with various salinity degrees and vegetation cover with different LAI densities were simulated and generated at the satellite-sensor level in VNIR and SWIR spectral bands of OLI. Thus, the examined VI's and evaporite indices were calculated and statistically analysed.

2.6. Landsat-OLI image pre-processing

Over Omongwa salt-pan site, the used Landsat-OLI image was acquired during the dry season the 28th of September 2016 (Fig. 3) by a very clear day without clouds or cirrus contaminated, and without shadow effects because topographic variations are absent in this area. Before processing and information extraction, pre-processing operations have been applied to this image (Teillet et al., 1994; Bannari et al., 1999). Indeed, radiometric sensor-drift calibration and illumination geometry were corrected to convert the DN to the apparent reflectances at the top of atmosphere using the irradiance, solar zenith and azimuthal angle values, and absolute calibration parameters (gain and offset) delivered by USGS-EROS Center in the image metadata file. Thereafter, the atmospheric interferences measured by the nearest meteorological station to the study site during the acquisition of image were integrated in CAM5S RTC to simulate and calculate the required atmospheric correction parameters for ground refelectances retrieval (Pahlevan et al., 2014). The implementation and application of these pre-processing operations were combined in one-step using PCI-Geomatica (PCI, 2018) to avoid multiple resampling and to preserve the radiometric integrity of the image data.

2.7. Spectra and image data processing

Theoretically, salinity indices (SI) must be highly sensitive to different salinity contents present in the soil surface, allowing only a qualitative assessment. Nevertheless, they can also be integrated into semi-empirical or physical models for quantitative prediction of the salinity content classes in the soil (Al-Ali et al., 2021). To select the most informative soil salinity index, comparative studies have been completed by applying regression analyses between $EC\text{-}_{Lab}$ and SI derived from spectral measurements, satellite, airborne and drone images (Allbed et al., 2014; Bannari et al., 2018; Peng et al., 2019; Hu et al., 2019; Wei et al., 2020; Milewski et al., 2020; Gopalakrishnan and Kumar, 2020). Often, obtained results vary depending on the spectral wavebands integrated in the equation of each index. For instance, in irrigated agricultural land in North Africa, the comparison among the SI discussed in the introduction above pointed out the very limited ability of these indices to differentiate between slight and moderate salinity classes (Bannari et al., 2016). But they have shown some potential to indicate the impact of soil salinity on the crop canopy stress. Considering a wide range of salinity contents (from slight to extreme) in arid landscape (Middle-East) (Shahid et al., 2010), these SI have poorly differentiated the salinity classes (El-Battay et al., 2017,

https://doi.org/10.5194/soil-2021-55
Preprint. Discussion started: 24 August 2021

Bannari et al., 2017b; Al-Ali et al., 2021). On the other hand, these studies showed that the SSSI integrating the SWIR bands provided the best sensitivity to the presence of salts in the soil. As well as the NDGI (or, SI-$_{ASTER\text{-}4,5}$) performed for evaporite minerals differentiation (Al-Khair, 2003; Milewski et al., 2019). Therefore, these two indices are considered in the present study and compared to the most popular and widely used VI's (NDVI, SAVI, EVI and TDVI) to characterize the salinity status in the soil surface. The six indices were implemented and calculated from simulated data and Landsat-OLI image using EASI-modeling of PCI-Geomatica software (PCI, 2018).

$$\mathrm{NDVI} = \frac{(NIR-R)}{(NIR+R)} \tag{1}$$

$$\mathrm{SAVI} = (1+L) * \frac{(NIR-R)}{(NIR+R+L)} \tag{2}$$

$$\mathrm{EVI} = 2.5 * \frac{(NIR-R)}{(NIR+6R-7.5B+1)} \tag{3}$$

$$\mathrm{TDVI} = 1.5 * \frac{(NIR-R)}{\sqrt{NIR^2+R+0.5}} \tag{4}$$

$$\mathrm{NDGI} = \frac{(SWIR1 - SWIR2)}{(SWIR1 + SWIR2)} \tag{5}$$

$$\mathrm{SSSI2} = \frac{[(\mathrm{SWIR1} * \mathrm{SWIR2}) - (\mathrm{SWIR2} * \mathrm{SWIR2})]}{\mathrm{SWIR1}} \tag{6}$$

Where: R and NIR are the ground reflectance in the red (OLI-4) and near-infrared (OLI-5) spectral bands, "L" is a correction factor equal 0.5; SWIR1 and SWIR2 are the ground reflectance in shortwave infrared spectral bands, OLI-6 and OLI-7 bands, respectively.

3. Results Analysis

3.1. Spectral and soil laboratory analyses

The spectral signatures of the measured 100 soil samples are presented in Fig. 4. These spectra show important changes in the reflectance's amplitudes and shapes highlighting several absorption features (position and depth). In the VNIR, they are influenced by several factors including mineralogical composition and assemblage, impurity, structure, size of salt crystals, and the soil optical properties (color brightness, texture, roughness, etc.). While, in the SWIR significant absorption features are influenced and controlled by the type and content of the salt mineralogy existing in each soil sample particularly the gypsum, sodium chloride (halite), calcium carbonate (calcite), and sodium bicarbonate (nahcolite). Since the impact of moisture content on the measured soil samples is completely

https://doi.org/10.5194/soil-2021-55
Preprint. Discussion started: 24 August 2021

absent or insignificant (0 to 0.05%), only weak absorption bands near 970, 1160, 1350, 1800, and 2208 nm were observed in some samples (atmospheric water vapor absorption features in 1440 and 1920 nm are not considered in this analysis).

Furthermore, the EC_{-Lab} revealed that the obtained values are distributed progressively in a wider range between 1.6 and 700 $dS.m^{-1}$, respectively, for agricultural fields and Sabkha "salt scald" consisting of pure salt (halite). These soil samples present high quantities of chloride (Cl^- : 9.6 to 3932 meq/l), sodium (Na^+: 23 to 3615 meq/l), magnesium (Mg^{2+}: 7.8 to 1118 meq/l) and calcium (Ca^{2+}: 39 to 230.4 meq/l) than other ions. The dominant ions in the soil samples are chloride (Cl^-) and sodium (Na^+) showing, respectively, an R^2 of 0.98 and 0.87 with EC_{-Lab}. While, the low relationship occurs with Ca^{2+} (R^2 of 0.23) and moderate with Mg^{2+} (R^2 of 0.48) and K^+ (R^2 of 0.46). The main sources of Cl^- in the soil are from seawater (level rise and spray), precipitation, salt dust, irrigation, and fertilization. Whereas, parent material, pedogenic processes, irrigation with saline-sodic waters and inappropriate soil drainage are the main sources of Na^+. Likewise, it is observed that the EC_{-Lab} and SAR increased gradually and very largely from non-saline (EC_{-Lab}: 1.6 $dS.m^{-1}$, SAR: 0.4) to extreme salinity in Sabkha (EC_{-Lab}: 700 $dS.m^{-1}$, SAR: 445), yielding an R^2 of 0.70 between each other. Moreover, the soil pH values ranged from 7 to 7.7 indicated slightly alkaline reaction due to the presence of bicarbonate (HCO_3^-) in the soils with a range from 4 to 10 $meq.l^{-1}$; as well as, the $CaCO_3$ ranged from 12.5 to 26% showing calcareous soil and parent materials, which significantly occurs in the arid regions. The results of these chemical analyses showed also the low quantities of organic matter (OM < 2.6%) in all soil samples, with an average of 0.58%. While the soil texture analysis showed an increase in salt content with a decrease in soil particle size, which obviously causing significant variation in the amplitude and the shape of the spectral signatures particularly in the VNIR. Definitely, this spectral confusion masked the effects of different salt contents in the soil. According to these laboratory analyses, we have a clear idea about the chemical components and their contents in each soil sample considered in this study.

3.2. Spectral and CRRS Analysis

To understand the impact of different salt contents on the spectral behaviour, among the 100 soil samples presented in Fig. 4 only eight samples are selected with different salinity contents. Their EC_{-Lab} range between 2.4 and 507 $dS.m^{-1}$, pHs between 7.35 to 8.10, and SAR vary from 1.6 to 444.7 $(mmoles/L)^{0.5}$. Fig. 5a illustrates their spectral signatures noted from A to H, and their characteristics descriptions are summarized in Table 1 (last eight samples in this table). These spectra show severe confusions in the VNIR regions, which are caused by the soil optical properties (i.e., color, brightness, texture, etc.) rather than the soil content in the soil. For instance, the reflectance spectra of sample "D" (195.3 $dS.m^{-1}$) coincide with that of sample "H" (507 $dS.m^{-1}$), although they do not have the same EC_{-Lab} values, because the soil characteristics play a fundamental role in this confusion (Fig. 5a and Table 1). In fact, the sample "D" is a sandy soil with small amount of gypsum crystals and shells, and the beginning of salt crust formation (light gray and white color), while the sample "H" is a pure salt-sabkha (bright florescent halite crust). Similar confusion is also observed between the opposite samples "A" and "H", respectively, with 2.4 and 507 $dS.m^{-1}$ values of EC_{-Lab}. Moreover, the samples "A" and "G" are sandy soils with EC_{-Lab} of 2.4 and 445.5 $dS.m^{-1}$, respectively; however, they exhibited approximately the same spectral behaviour and amplitude in the VNIR

https://doi.org/10.5194/soil-2021-55
Preprint. Discussion started: 24 August 2021

according to their color (Fig. 5a and Table 1). Consequently, it is impossible to discern or to separate between "D" and "H" or "A" and "G" samples in the VNIR. This affirmation was also reported by Metternicht and Zinck (1997), who demonstrated that the soil textures can be a source of spectral confusion between soil salinity classes; as well as the color and roughness of the soil crusts influenced the reflectance in VNIR and, therefore, causing confusion among the salts contents in the soil.

On the other hand, the Fig. 5a shows that when the EC_{-Lab} values increase, also the difference among the salt-affected soil spectra's increase significantly and progressively from 1100 to 2500 nm region of the spectrum. In this SWIR domain, the spectral signatures of soil samples from "A" to "H" changed progressively in amplitude and shape according to EC_{-Lab} contents (from 2.4 to 507 dS.m^{-1}, see Table 1), as well as a function of SAR (from 1.6 to 444.7 (mmoles/l)$^{0.5}$). The ambiguity between "D" and "H" or "A" and "G" samples observed in the VNIR, is completely dismissed in the SWIR and it is easy to see gradually the spectral signature position of each sample according to its EC_{-Lab} content. Definitely, the two SWIR bands of OLI show the highest potential to discriminate efficiently among different degrees of salinity in the soil (Fig. 5a). These results corroborate those of other researchers who had shown, for instance, that pure salt (halite, NaCl) does not induce absorption features in the VNIR (Hunt et al., 1971), and other authors reported some absorption features in SWIR wavebands around 1400, 1900, and 2250 nm (Fig. 5a) that are attributed to dissolved salt in soil moisture and existing liquid in the soil (Mougenot et al., 1993; Howari et al., 2002a). Moreover, Howari et al. (2002b) and Farifteh (2007) showed that the depth of absorption features increased with increased salt content in the soil.

[Table 1]

Furthermore, the CRRS transformation of the eight considred soil samples (Table 1) are illustraed in the Fig. 5b. A total absence of absorption features is observed between 525 and 920 nm, but some features between 350 and 525 nm are revealed. Unfortunately, in this portion of wavelenghts that include the blue band of OLI is not conclusive because the increase in salinity content does not mean a significant and separate features among soil salinity classes. Indeed, in this specific electromagnetic window we observe that the sample "H" which is 10 time more saline than the sample "B" (EC_{-Lab} of 507.0 and 50.5 dS.m^{-1}, respectively) are showing similar absorption features. Moreover, the samples "A", "C" and "E" with different salinity conetnts (EC_{-Lab} of 26.2, 90.0 and 381.0 dS.m^{-1}, respectively) are presenting comparable absorption features (Fig. 5b). This similarty is automatically related to the texture, raughness, color and brightness of soil samples and not for their salinity content degrees. Infact, "B" and "H" samples have the same color (white, 10YR 8/1), while the samples "A", "C" and "E" are presenting a very slight mixt color and brigtness (white-beige, light-gray and light-gray-white) but showing similar Mensel color (10YR 7/2, Table 1). Moreover, CRRS pointed out that no absorption features charaterizes the salinity in the red and NIR bands (Fig. 5b). Therefore, this spectral transformation (CRRS) corroborates the original spectral signatures behaviour which means the impossibility to discriminate among soil salinity classes in VNIR spectral domains. Otherwise, numerous and significant absorption bands are observed between 920 and 2500 nm highlighting the more suitability of SWIR wavebands for soil salinity discrmination (i.e., absorption features beyond 950 nm were broadened). In

https://doi.org/10.5194/soil-2021-55
Preprint. Discussion started: 24 August 2021

fact, CRRS has shown that increases in soil salinity (EC_{-Lab}) induced automatic changes in the depth of absorption features, particularly in the water absorption bands, which were shifted toward shorter wavelengths. Consistent absorption features are observed at wavelengths of 980, 1175, 1448, 1933, and 2430 nm particularly for the pure salt (sodium chloride) and gypsum samples. These results are in agreement with the findings of Dehaan and Taylor (2002) and Farifteh (2007).

[Figure 5]

Otherwise, Fig. 6a illustrates the measured spectral signatures of vegetation cover samples at different LAI rates. These typical spectra of healthy vegetation show the absorption of the visible electromagnetic radiation by the photosynthetic pigmentation in plants tissues (i.e., carotenoids and chlorophyll). It is well known that each pigment has different spectral absorption features allowing remote sensing to assess vegetation conditions and, therefore, give an indication of its overall physiological state (Bannari et al., 2007 and 2008b). The red-edge transition region between the visible and NIR, from 675 to 750 nm, is informative about vegetation cover diseases and early detection of pest-attacks (Thenkabail et al., 2018). While in the NIR, a large fraction of the incoming electromagnetic radiation is reflected toward space according to the biomass density. As we discussed before and also reported by other studies (Thenkabail et al., 2004; Pacheco et al., 2008), the VNIR spectral domains are the most prominent regions for green vegetation cover discrimination and the most used in VI's equations. Whereas, in the SWIR wavelengths, the solar radiation is absorbed by the water content available in the canopy. These wavebands are indicators of water stress due to water-deficiency in the canopy (Gao et al., 1996; Champagne et al., 2003). Furthermore, the CCRS emphasizes the wavelengths where significant and gradual changes occurred depending on the LAI density (Fig. 6b), as well as on the carotene and chlorophyll contents particularly in the blue and red bands (Fig. 6b). Exceptions occur in the red-edge region (from 675 to 750 nm), and part of NIR spectrum (from 750 to 900 nm), where absorption features are absent. However, at the shorter wavelengths of the NIR from 935 to 1300 nm, some narrow bands appear characterizing water absorption features. While, stronger absorption features are observed after 1350 nm (1400-1800 and 1950-2350 nm) due to the variability of internal water content. Therefore, the subject covered in this section is evident and basically well known by remote sensing community. However, it is very important to show for the users that the spectral behaviour caused by the internal variability of bio-physiological parameters (carotenoids, chlorophyll, and water) of vegetation cover is completely different to that due to the evaporite minerals in VNIR and SWIR wavebands as illustrate by the Figs. 5 and 6.

[Figure 6]

3.3. Indices validation based on simulated data and measured EC_{-Lab}

In this section, the analysis of VI's capability for soil salinity discrimination was undertaken in two different ways. The first involves a 2D spectral-space analysis (scatter-plot) relating each index to the reflectance in the red band (Fig. 7). Among the 100 sampled soils, only 20 samples are considered in this analysis. Their EC_{-Lab} values are

https://doi.org/10.5194/soil-2021-55
Preprint. Discussion started: 24 August 2021

ranging from 2.4 dS.m^{-1} (non-saline soil) to 635 dS.m^{-1} (pure salt, sabkha), and their characteristics are summarized in Table 1. The 2D spectral-space illustrates how the fraction of vegetation cover is perfectly highlighted by the VI's (Fig. 7), and predicted correctly and gradually from 50% to 95% proportionally to the increased LAI rates. Whereas bare soil samples are compressed towards the hypothetical soil-line (Jackson et al., 1983; Huete et al., 1994a and 1994b; Bannari et al., 1996) with null values regardless of their salt content. Indeed, they are quantified by VI's considering their color in a very limited range values between 0% and 8% for very salty soils with dark and bright color, respectively. Consequently, undoubtedly VI's cannot exhibit the spatial patterns variability or provide precise and reliable information about the soil salinity. This finding corroborate those of spectral and CRRS analyses. Accordingly, if these indices compress and/or eliminate signals coming from the underlying soils, how is it possible for theme to discriminate the salinity classes, particularly in a large OLI pixel area of 900 m^2 with mixt information of salty soil and vegetation cover fraction?

[Figure 7]

Furthermore, the second part of this analysis considers the totality of 100 soil samples applying a first order polynomial regression ($p < 0.05$) between the measured EC-$_{Lab}$ and predicted salinity based on the examined VI's (Fig. 8). Obtained results showed insignificant fits for SAVI, EVI and TDVI ($R^2 \leq 0.06$), as well as for NDVI (R^2 of 0.35). Once more, these statistical fits corroborate the spectral signatures and 2D spectral-space analyses, and the CRRS transformations results that VI's based on VNIR wavebands are not appropriate for correct and accurate discrimination among various soil salinity classes. Unlike VI's, the evaporite minerals indices have the highest power for soil salinity discrimination with R^2 of 0.71 and 0.72 for NDGI (or SI-$_{ASTER-4,5}$) and SSSI (Figs. 8e and 8f), respectively. These results are due to the absorption features of salts (gypsum, halite, etc.) in SWIR bands, which are integrated in the equations of the both indices. Overall, the results are satisfactory and consistent with previous studies. Indeed, in irrigated agricultural land with slight and moderate salinity, the validation of SSSI derived from ALI EO-1 with respect to the ground truth showed an excellent fit with R^2 of 0.96 (Bannari et al., 2016). Al-Khaier (2003) showed a good potential of NDGI named also SI-$_{ASTER-4,5}$ (R^2 of 0.86) for soil salinity detection in irrigated agricultural land in Syria using ASTER and ETM+ images. On the basis of spectral measurements of soil samples collected from Omongwa salt-pan, Milewski et al. (2019) have demonstrated the performance of NDGI for gypsum content prediction (R^2 of 0.84). However, they have shown that this capacity varies with the spatial and spectral characteristics of the image data used and other sources of problems. Indeed, when NDGI was extracted from airborne (HySpex) and satellite (Hyperion) hyperspectral images acquired over the pan, the obtained fits showed an R^2 of 0.79 for HySpex with 2.4 m pixel size compared to R^2 of 0.71 for Hyperion with 30 m pixel size. Eventually, this variability can be caused by several problems including the mixture of mineral component fractions within the pixel size, the low-quality of sensor SNR especially for Hyperian (Kruse, 2001), the residual errors of atmospheric absorption (Khurshid et al., 2006), the sensitivity of SWIR wavebands to some fragments of senescent vegetation (i.e., absorption by cellulose and lignin) (Bannari et al., 2015), and the specular effect caused by BRDF problems

https://doi.org/10.5194/soil-2021-55
Preprint. Discussion started: 24 August 2021

(Mishra et al., 2014). However, despite these small variations, the NDGI successfully completed its mission providing satisfactory results.

[Figure 8]

3.3. Derived soil salinity maps analysis

For the interpretation, analysis and validation of the salinity maps derived from Landsat-OLI image acquired over Omongwa salt-pan site, 14 soil samples collected from the top-surface representing mineralogical ground truth classes were used (Table 2). These points were sampled and analysed in 2014 and 2015, and published by Milewski et al. (2017). Moreover, since the soil salinity dynamics occur in response to the way that water moves through and over the landform following the terrain morphology and topography under the gravity effects (Moore et al., 1993; Kinthada et al., 2013; Bannari et al., 2021), an accurate Lidar DEM was used (Fig. 9). Generated with a spatial resolution of 1 m and a vertical accuracy of ±10 cm (Milewski et al., 2017), this DEM undoubtedly supports our understanding of the topographic impact on the spatial distribution of salinity classes across the pan site. A transects (A-B) traced from southwest to northeast on the DEM shows the elevation variation between 1227.00 and 1227.80 m with a convex shape and a depth of 80 cm promoting water accumulation, particularly in centre-east and north-east (Fig. 9).

[Table 2]

[Figure 9]

Fig. 10 illustrates the soil salinity maps derived based on NDVI, SAVI, EVI and TDVI. It is observed that these indices are blind and unable to detect the presence of salinity in the middle or at the edges of Omongwa pan, although it is natural flat salt crust playa as shown in Fig. 3. These cartographic products visually corroborate the results obtained through the analyses of 2D spectral-space (scatter-plots) and CRRS, as well as the statistical fits with $EC_{\text{-Lab}}$. In the center, north and east of the pan some non-classified pixels (black pixels) are due to the absence of signals that are absorbed by the accumulated water in low topographic areas. Faithful to their mission of detecting the presence of vegetation, these indices maps are highlighting the presence of scattered halophytes in the peripheral neighbourhood (north-east and east) of the pan playa. Obviously, this is wrong information about soil salinity outside the salt-pan. In fact, these results were anticipated because in remote sensing domain it is well known that the primordial and main mission of VI's is the detection and characterization of photo-synthetically active vegetation cover as discussed before. Further, they cannot provide any information about the soil because their basic concept removes the contribution of the soil background from the total signal remotely sensed at the top of atmosphere as shown in the simulation results. However, in contrast to these results some scientists claim the predictive power of VI's for soil salinity discrimination and mapping. For instance, Allbed et al. (2014) found that the SAVI extracted from the IKONOS image is useful for assessing the soil salinity in areas dominated by date palm

https://doi.org/10.5194/soil-2021-55
Preprint. Discussion started: 24 August 2021

trees. On the other hand, when analyzing vegetation cover growth over agricultural lands in South Dakota based on the time series of MODIS VI, Lobell et al. (2010) observed that EVI was significantly correlated with soil salinity and more sensitive to changes in salinity stress than NDVI. While, over agricultural soils in California, Whitney et al. (2018) showed that the temporal interpretation of the time series of MODIS VI's can probably be used to measure the canopy response to stress caused by soil salinity. Contrary to the conclusions of Lobbel et al. (2010), Whitney et al. (2018) observed that the strength of the correlation coefficients between VIs and salinity was generally better for NDVI than for EVI.

[Figure 10]

In the PCI-Geomatica image processing system, the histograms of the derived salinity maps applying SSSI and NDGI (Fig. 11) were thresholded based on the major salinity classes including non-saline (blue), low (cyan or sky-blue-green), moderate (clear green), high (yellow), very high (orange-red) and extreme salinity (red-purple). Indeed, the values of the centroids of the clusters representing these classes were considered; as well as, the standard deviation value was chosen to limit the overlap between the classes considered and to reduce the chance of a pixel being classified into more than one class. Fig. 11 shows the spatial distribution of salinity classes across the study area and in the outer-peripheral regions of the pan. In general, it is observed that the both indices (SSSI and NDGI) mapped the salinity patterns almost similarly by reflecting the results of the statistical fits discussed above. However, although the NDGI detects the presence of salinity, it further highlights the gypsum content; particularly in the borders of the pan (i.e., south, southwest, and north). While, the SSSI further highlights the main salt crusts present in the pan area that are formed from different mineral sources, including halite, gypsum, calcite, and sepiolite; as reported ago two decades by Mees (1999) and also recently confirmed by Milewski et al. (2017 and 2019). Moreover, these results are logical since the less soluble carbonates can be found at the edge of the pan, followed by a succession of sulphates to chlorides towards the central area with lower topography as shown by DEM (Shaw and Bryant, 2011).

[Figure 11]

Furthermore, the 14 points representing the ground truth (Table 2) are used for the results validation and analysis process. Their mineralogy is dominated by halite (which appears as white bright and florescent salt crust surface in Fig. 3), followed by the gypsum as a second most abundant crust (Table 2). Their EC_{-Lab} values are ranging between 17.6 and 129.7 $dS.m^{-1}$, and the pH is greater than 8.2 reflecting a strong sodicity coupled with salinity. Superimposed on salinity maps derived by NDGI and SSSI indices (Fig. 11), most of these points coincide perfectly with areas showing a high content of salt or gypsum, particularly in the southern borders of the playa. Following the topographic characteristics of the pan area, a total absence of salinity is observed in the center and center-east parts of the pan (black pixels) due to the presence of water which absorbs the signal in the SWIR wavelengths. While in the south and north-western of central part, where the topography is slightly raised, moderate and high salinity

https://doi.org/10.5194/soil-2021-55
Preprint. Discussion started: 24 August 2021

classes are noted by the both indices but more emphasized with SSSI than NDGI. Indeed, because the halite crust covers the majority of pan playa surfaces, inside and outside, with variable contents. Whereas, the gypsum-halite crust mixture surrounded the border as a natural boundary between the interior and the peripheral margin of the pan highlighting a very high to extreme salinity class caused, probably, by the displacement of salt from the surface to the playa edges due to wind action and erosion, as well as by human movements (Bryant, 1996). Moreover, it is also observed that high, very high and extreme salinity classes are associated with slightly high elevation.

According to mineralogical ground truth, the validation points P63, P64, P65 and 172 in the southern region of the pan are dominate by the gypsum crust (33% to 83%) associated with a small amount of halite (5% to 36%). This terrain truth is detected and well mapped by the two indices, but NDGI highlighted more the gypsum belt in south and southwest (Fig. 11). In this region the topography is slightly high and decreases toward the centre-east of the pan, and then it becomes relatively higher in the north and north-west. Points P66 and P67 located on a small circular ridge in the south-central part of the pan with a slight elevation, have almost similar contents of halite and gypsum (45%). However, the salt content in these two points is more stressed in the SSSI map. As well as, nearby points 143 dominated by halite (52%) followed by gypsum (38%) and point 171 with 50% of halite and 27% of quartz, the SSSI map shows more sensitivity to this class than that of NDGI (Fig. 11). The zone surrounding sample point 141 which is nearly pure halite (94%) mixed with very low content of gypsum (3%) is better enhanced by SSSI than NDGI.

Further north of the pan site, areas around the validation points P69, P70 and P71 located at slightly high elevation (~ 1227.8 m) are mapped as very high to extreme salinity classes by SSSI, which also indicates that overall there is an important increase of the salt content in this northern space. These results can be explained by the fact that the SSSI is more sensitive to the halite crust accumulated on the surface which is exposed and clearly visible to the FOV of the Landsat-OLI from space; while the other minerals (less soluble) are precipitated under the layer of halite (Chivas, 2007). The NDGI predict this zone as a moderate salinity class because the mineralization nearby these points indicates the absence or slight content of gypsum and a main mixture of quartz, halite, calcite and sepiolite (Table 2). Indeed, this region was mapped by Milewski et al. (2017) as combined fractions of calcite and sepiolite based on linear spectral mixture analysis (LSMA), hyperspectral imagery and measured endmembers in the field. Nevertheless in the present study, the evaporite indices are applied to the broad bandwidth of the OLI sensor which does not allow the extraction of mineralogical fraction maps like LSMA, but rather a map of salinity showing all salt minerals existing at the surface of study area. However, the results obtained here are very satisfactory and very similar to those obtained by LSMA but all the fractions are combined in one and unique extreme salinity class. Likewise, the results obtained by NDGI in the present study using the OLI image acquired in September 2016 are generally quite similar to those obtained by Milewski et al. (2017). However, only minor differences are observed between the results of these works, because the pan center is heterogeneous and highly dynamic in time (Schuller et al., 2018).

The outer region of the pan, particularly in the east and north, exhibits different salinity classes ranging from moderate to extreme are, probably, associated with wind and dust-storm processes. Indeed, Aeolian salts occur in arid lands consequently through the erosion of salt playa surfaces transported by wind (high concentrations of fine-

https://doi.org/10.5194/soil-2021-55
Preprint. Discussion started: 24 August 2021

grain of salt) and deposited in this area forming sandy-salt-encrusted surfaces. The areas covered by these classes are certainly located geographically in zones where the wind and sand-storms speed is high. According to Abuduwaili et al. (2010), the main source of saline dust is the abundance of unconsolidated salt located in enclosed basins that are affected by strong wind and human disturbance. This type of salinity source has also been widely observed in the arid Australian landscapes (Zinck and Metternicht, 2009), in the desert of Gobi in China-Mongolia border region (Wang et al., 2012), in eastern Asia and western Pacific (Zhu and Yang, 2010), in dry playas in the Mojave Desert, USA (Reynolds et al., 2007), in the shorelines of the Salton Sea in California (Buck et al., 2011), Aral sea basin-Uzbekistan (Xenarios et al., 2020) and in the deserts of Kuwait (Bannari and Al-Ali, 2020). Moreover, Aeolian processes were also identified as important salt sediments transport processes in salt playa in semi-arid south-central of Tunisia (Millington et al., 1989).

4. Discussion

The chemical analyses of the 100 examined soil samples disclosed high quantities of chloride (Cl^-), sodium (Na^+), magnesium (Mg^{2+}) and calcium (Ca^{2+}). Nevertheless, the chloride and sodium contents fitted very significantly with EC_{-Lab}, R^2 of 0.98 for Cl^- and 0.87 for Na^+. It is also revealed that the EC_{-Lab} and SAR values changed progressively in a wider ranges between non-saline samples (EC_{-Lab} = 1.6 dS.m^{-1}, and SAR = 0.4) collected from agricultural fields and extreme saline soils (EC_{-Lab} = 700 dS.m^{-1}, and SAR = 445) sampled from pure salt (halite) and gypsum in Sabkha. Moreover, the spectral signatures of the considered soil samples illustrate important changes in the reflectance's amplitudes and shapes (Fig. 4). They revealed severe confusions in the VNIR, which are caused by the soil optical properties rather than the soil salinity contents. These observations are consistent with the results of other researchers (Irons et al., 1989; Huete 1989; Metternicht and Zinck, 2003; Bannari et al., 1996 and 2018). While, the spectra pointed out several absorption features that are linked to the salt mineralogy including gypsum, halite, calcite and nahcolite, especially in the SWIR wavebands as reported by other scientists (Csillag et al., 1993; Howari et al., 2002a; Katawatin and Kotrapat, 2005; Farifteh et al., 2008; Mashimbye, 2013; Bannari et al., 2018; Al-ali et al., 2021). For example, pure halite (NaCl) is transparent and its chemical composition and structure does not show any absorption features in the VNIR spectral domains, corroborating the finding of Hunt et al. (1971 and 1972). Whereas, absorption bands near the 1420, 1920, and 2250 nm in the spectra of halite are attributed to moisture and fluid inclusions, as also reported by several authors (Crowley, 1991; Mougenot et al., 1993; Howari et al., 2002a; Farifteh, 2007).

The CCRS transformations corroborate the trends of spectral signatures and highlighted the confusions in the VNIR that are caused by the soil optical properties rather than the salt contents in the soil. For instance, very severe confusion is noted between the soils samples "A" with EC_{-Lab} of 2.4 dS.m^{-1} and "G" with 445.5 dS.m^{-1}; despite this important difference in salt contents they exhibit approximately the same spectral behaviour and amplitude in the VNIR according to their color and texture (Fig. 5a and Table 1). Consequently, it is impossible to discern or to separate between soil salinity classes in the VNIR. While when the EC_{-Lab} values increased also the difference among the salt-affected soil spectra's increased significantly and progressively in the SWIR (Fig. 5a). In this spectral region, the spectra of soil samples "A" to "H" changed progressively in amplitude and shape due to the

https://doi.org/10.5194/soil-2021-55
Preprint. Discussion started: 24 August 2021

increasing values of EC-$_{Lab}$ (from 2.4 to 507 dS.m^{-1}). Nevertheless, the noted ambiguity between "A" and "G" samples in the VNIR is completely dismissed in the SWIR. Indeed, it is easy to see gradually the spectral signature position of each sample according to its EC-$_{Lab}$ content; as well as, the CRRS has shown that increases in soil salinity (EC-$_{Lab}$) induced automatic changes in the depth of absorption features. For instance, CRRS analyses of halite-rich soil "H" sample showed consistent absorption features at 960, 1160, 1420, 1780 and 1920 nm and they become deeper, broader, and more asymmetrical with increasing salt content in the soil. Based on several statistical analyses including CRRS, spectral matching techniques, hierarchical classification, and Mann–Whitney U-test; Farifteh (2007) demonstrated rigorously that the SWIR spectral domain contain the most crucial information about soil salinity differentiation. These findings are in agreement with the results of other scientists who characterized several soils rich in sulfates minerals, carbonates and bicarbonates, sodium chloride, etc. (Bowers and Hanks, 1965; Mougenot et al., 1994; Verma et al., 1994; Owen, 1995; Howari et al., 2002a and 2002b; Farifteh et al., 2008; Weng et al., 2008; Masoud, 2014; Nawar et al., 2015; Neto et al., 2017; Bannari et al., 2018; Milewski et al., 2019). Accordingly, the SWIR-1 and SWIR-2 bands of OLI show the highest potential to discriminate efficiently among different degrees of salinity in the soil.

Otherwise, spectral analysis and CCRS transformation of LAI at different densities confirmed the relevance of VNIR and SWIR for the assessment of the vegetation cover from viewpoints of biomass, physiological pigmentation and stress. In addition, the 2D spectral-space analysis highlighted the primordial utility of VI's to differentiate the vegetation covers perfectly proportionally to their LAI rates. Unfortunately, the investigated VI's compress the bare soils samples towards the hypothetical soil-line with null values regardless of their salt contents. These irrelevant results are in agreement with those of spectral and CRRS analyses, since VI's are based on blue, red and NIR bands that are not conclusive for soil salinity differentiation. Moreover, statistical regressions ($p <$ 0.05) between the measured EC-$_{Lab}$ and predicted salinity based on VI's are very insignificant for SAVI, EVI and TDVI ($R^2 \leq 0.06$), as well as for NDVI (R^2 of 0.35). Certainly, these simulations in an ideal and controlled environment lead to rigorous validation and comparison procedures between the considered indices. In fact, atmospheric interferences are absent, SNR is high, fragments of senescent vegetation are absent, salt contents are well known in soil samples and, consequently, the results obtained are optimal and realistic. These finding are consistant with other results obtained by some researchers who fitted EC-$_{Lab}$ with VI's derived from simulated data, satellite or drone images. For instance, Golabkesh al. (2021) obtained very weak relationship with NDVI (R^2 of 35%), Ferdous and Rahman (2017) revealed insignificant fit ($R^2 \leq 0.03$) with SAVI and NDVI, and Zhang et al. (2011) demonstrated also a low regression trend ($R^2 < 0.28$) for NDVI. These weaknesses are mainly due to the ambiguous information about soil salinity in the VNIR bands. Moreover, based on spectral data and Landsat-OLI image, Al-Ali et al. (2021) demonstrated that the soil salinity models integrating VI's and/or the VNIR bands are inappropriate and inaccurate to predict soil salinity.

Over the Omongwa salt-pan site, although the higher albedo of the site centre in the image is principally due to halite crust developed and accumulated during many years as illustrated by true color composite RGB of Landsat-OLI image (Fig. 3), the derived soil salinity maps using VI's are completely unable to detect the slightest grain of salt in the soil. Obviously, the visual analysis of these maps validate and corroborates the previous analyses (i.e.,

https://doi.org/10.5194/soil-2021-55
Preprint. Discussion started: 24 August 2021

spectral, CCRS, 2D spectral-space, and statistical fits) based on simulated data. Obviously, these results were anticipated knowing that the primordial and main mission of VI's are the detection and characterization of vegetation canopy by removing the contribution of the soil background from the signal remotely sensed at the top of atmosphere. Probably, it is possible for VI's to anticipate the vegetation canopy stress caused by the underlying soil salinity (Lobell et al., 2010; Zhang et al., 2011; Bannari et al., 2016; Whitney et al., 2018), but they do not have the ability to discriminate and predict soil salinity classes. Definitely, the widespread use of VI's carries inherent risks misuse by users who exploit remote sensing as a tool, and who have received little or no education in remote sensing domain (Huang et al., 2020). Indeed, remote sensing is not limited to the story of having an image processing software packages and free satellite images, but it is a multi-disciplinary and multi-concept scientific fields. It is based on complex comprehension of a wide range of electromagnetic radiation, reflected or emitted, and its interaction with the biosphere-atmosphere environment. Hence the interest of this research to investigate whether the potential of VI's for soil salinity discrimination is a myth or a reality.

Furthermore, considering the simulated data over Kuwait site or the Landsat-OLI image acquired over Omongwa salt-pan, SWIR wavebands are distinguished by their potential to differentiate among several salt contents in the soil. The spectral signatures analysis and CRRS transformation showed that increases in soil salinity ($EC\text{-}_{Lab}$) induced automatic changes in the depth of absorption features in SWIR. Statistical regressions between the $EC\text{-}_{Lab}$ and evaporite mineral indices showed an excellent and similar discriminating power (R^2 of 0.72) for NDGI and SSSI (Figs. 8e and 8f). Moreover, the salinity maps derived by these two indices illustrate a good spatial distribution of salinity classes across the study area and in the outer-peripheral regions of the pan (Fig. 11). The both indices mapped the spatial distribution of salinity patterns almost similarly, corroborating the results obtained from simulated data and statistical fits discussed above. Overall, the validation of these maps shows a good agreement with the field truth. However, although the NDGI detects the presence of salinity, it further highlights the gypsum content; particularly in the borders of the pan (i.e., south, southwest, and north). While, the SSSI further highlights the main salt crusts present in the pan area that are formed from different mineral sources, including halite, gypsum, calcite, and sepiolite; as reported by Mees (1999) and confirmed by Milewski et al. (2017 and 2019). In general, these results are due to the absorption features of salts (gypsum, halite, etc.) in SWIR bands, which are integrated in the equations of the both indices. Likewise, Al-Ali et al. (2021) showed that the soil salinity models integrating the SWIR wavebands are the most promising for predicting and quantifying the salt-affected soil classes. Obviously, the results obtained in the present study are accomplished from Landsat-OLI data but they can also be achieved from Sentinel-MSI because we demonstrated that these two sensors can be used jointly to monitor accurately the soil salinity and it's dynamic in time and space in arid landscape (Bannari et al., 2020).

5. Conclusions

In the present study, we analyzed the potential and limits of vegetation indices compared to evaporite mineral indices for soil salinity discrimination and mapping in arid landscapes. To achieve these, combined approaches that exploit simulated spectral data and OLI image acquired over two study sites were used. The first site is the Kuwait-State in Middle-East and the second site is the Omongwa salt-pan in Namibia. Field survey was organized and 100

https://doi.org/10.5194/soil-2021-55
Preprint. Discussion started: 24 August 2021

soil samples with various salt contents were collected, as well as samples of vegetation covers with different LAI densities. Spectroradiometric measurements were acquired in a Goniometric-Laboratory above the soil and vegetation samples using the ASD spectrometer. To understand the complexity of the close relationship between the salt contents in the soil and their spectral signatures, soil chemical analyses were accomplished. Indeed, soluble cations and anions, pH and EC_{-Lab} were measured, and the SAR was calculated. Furthermore, the spectra of the most representative soil salinity classes and LAI densities were transformed using the CRRS. Likewise, all measured spectra were resampled and convolved in the solar-reflective spectral bands of OLI sensor. Afterwards, the indices were calculated and analysed in 2D spectral-space, and fitted statistically ($p < 0.05$) with EC_{-Lab}. Moreover, the acquired OLI image over Omongwa salt pan site was pre-processed and converted to the considered indices. Accurate Lidar DEM was used to support visual analysis and interpretation, as well as mineralogical ground-truth information collected and analysed previously were considered for the characterization and validation of the derived maps on this second site.

The results show that the soil spectral signatures are very sensitive to soil salinity contents. Their shapes, forms and amplitudes changed gradually depending on the salt contents (EC_{-Lab}). According to chemical soil laboratory analyses, the measured amounts of EC_{-Lab} in the examined soil samples are due to the chloride, sodium, magnesium and calcium which pointed out several absorption features in the spectra, particularly in the SWIR wavebands. On the other hand, it is also observed that the soil optical properties (color, brightness, texture, roughness, etc.) have an impact on these spectra, especially in the VNIR spectral domains. Overall, spectral analysis and CCRS transformation highlighted severe confusions of soil salinity classes in the VNIR wavelengths due to soil artefacts rather than the salt contents. Moreover, they revealed that blue band integrated in EVI equation is inconclusive for soil salinity differentiation, and the salts minerals absorption features are completely absent in the red and NIR bands that are generally used by VI's. While the SWIR wavebands show the highest potential for efficient discrimination among soil salinity classes.

Furthermore, spectral signatures analysis and CRRS transformation showed that the VNIR and SWIR fulfill their essential conditions to be sensitive to vegetation cover density and its physiological constituents. In addition, 2D spectral-space investigation results highlighted the primordial utility of VI's to differentiate the vegetation covers perfectly and proportionally to rates of LAI. While, regardless the salt contents in the soil samples, VI's are not conclusive as their fundamental concept eliminates the underlying soil contribution on the remotely sensed signal. These unsuccessful results are corroborated by statistical fits ($p \leq 0.05$), between the measured EC_{-Lab} and VI's, who achieved very low coefficients of determination, $R^2 \leq 0.06$ for SAVI, EVI, and TDVI, and R^2 of 0.35 for NDVI. Likewise, although the higher albedo of Omongwa salt-pan site due to halite crust developed and accumulated over years, the soil salinity maps derived from OLI image based on VI's are completely unable to detect the slightest grain of salt in the soil. Overall, regardless the data used, the processing method, the study site and the validation procedures, the results obtained converge toward the same conclusions that it is impossible for VI's to detect the spatial patterns variability or to provide precise and reliable information about the soil salinity classes.

Finally, considering the simulated data over Kuwait site, statistical regressions between the measured EC_{-Lab} and the evaporite mineral indices showed significant discriminating power (R^2 of 0.72) for NDGI and SSSI. Moreover,

https://doi.org/10.5194/soil-2021-55
Preprint. Discussion started: 24 August 2021

the derived maps from the OLI image based on these two indices over Omongwa salt-pan surface illustrated a good spatial distribution of salinity classes across and in the outer-peripheral regions of the pan site. Overall, the validation of these maps shows an excellent agreement with the field truth. However, although the NDGI detects the presence of salinity, it highlights the gypsum content; particularly in borders of the pan (i.e., south, southwest, and north). While, the SSSI further accentuates the main salt crusts present in the pan area that are formed from different mineral sources, including halite, gypsum, calcite, and sepiolite. In general, these results are due to the absorption features of gypsum and halite in SWIR bands, which are integrated in the equations of the both indices. Accordingly, NDGI and SSSI can be used to predict and monitor soil salinity and its dynamics in time and space in arid landscapes.

6. Author Contributions: Professor A.Bannari performed the paper conceptualization, data collection, pre-processing and processing, results analyses and paper writing. Professor A. Abuelgasim assisted in the results analyses and the paper writing. All authors have read and agreed to the published version of the manuscript.

7. Competing Interests: The authors declare no conflict of interest.

8. Acknowledgments

The authors would like to thank Dr. Shabbir A. Shahid (soil scientist specialist) from Kuwait Institute for Scientific Research (KISR) for the assistance during the soil laboratory analyses and for the review of this paper. They acknowledge the NASA-USGS for Landsat data and they express their gratitude to the anonymous reviewers for their constructive comments.

9. References

Abuduwaili, J., Liu, D., and Wu, G.: Saline dust storms and their ecological impacts in arid regions. J. Arid. Land, 2, 144–150. doi:10.3724/sp.j.1227.2010.00144, 2010.

Abuelgasim, A., and Ammad, R.: Mapping soil salinity in arid and semi-arid regions using Landsat-8 OLI satellite data. Remote Sensing Applications: Society and Environment, 13, 425-425, 2019.

Al-Ali, Z. M., Bannari, A., Rhinane, H., El-Battay, A., Shahid, S. A., and Hameid, N.: Validation and Comparison of Physical Models for Soil Salinity Mapping over Arid Landscape Using Spectral Reflectance Measurements and Landsat-OLI data. Remote Sensing, 13(3), 494, pp. 1-26. https://doi.org/10.3390/rs13030494, 2021.

Aldakheel, Y.: Assessing NDVI Spatial Pattern as Related to Irrigation and Soil Salinity Management in Al-Hassa Oasis, Saudi Arabia. J. Indian Soc. Remote Sens. 39(2):171–180, 2011.

Alexakis, D. D., Daliakopoulos, I. N., Panagea, L. S., and Tsanis, I. K.: Assessing soil salinity using WorldView-2 multispectral images in Timpaki, Crete, Greece. Geo-carto International, 33(4), 321-338, 2016.

Al-Khaier, F.: Soil salinity detection using satellite remotes sensing. Master's thesis, International institute for Geo-information science and earth observation, Enschede, The Netherlands, 61 pages, 2003.

https://doi.org/10.5194/soil-2021-55
Preprint. Discussion started: 24 August 2021

Allbed, A., Kumar, L., and Aldakheel, Y.Y.: Assessing soil salinity using soil salinity and vegetation indices derived from Ikonos high-spatial resolution imageries: Applications in a date palm dominated region. Geoderma, 230, 1-8, 2014.

Al-Sarawi, M.: Surface Geomorphology of Kuwait. Geo. Journal, 35(4), 493-503, 1995.

Arrouays, D., Lagacherie, P., and Hartemink, A.E.: Digital soil mapping across the globe. Geoderma Reg., 9, 1–4, 2017.

ASD: User Manual, http://support.asdi.com/Document/Viewer.aspx?id=162, 2015.

Asfaw, E., Suryabhagavan, K. V., and Argaw, M.: Soil Salinity Modeling and Mapping Using Remote Sensing and GIS: The Case of Wonji Sugar Cane Irrigation Farms, Ethiopia. J. of the Saudi Society of Agricultural Sciences, 1-9, 2016.

Azabdaftari, A., and Sunar, F.: Soil Salinity Mapping using Multi-temporal Landsat Data. The International Archives of the Photogrammetry, Remote Sensing and Spatial Information Sciences, Volume XLI-B7, 2016 XXIII ISPRS Congress, 12–19 July 2016, Prague, Czech Republic, pp. 3-9. doi:10.5194/isprsarchives-XLI-B7-3-2016, 2016

Bannari, A.: Synergy between Sentinel-MSI and Landsat-OLI to Support High Temporal Frequency for Soil Salinity Monitoring in an Arid Landscape, In: Research Developments in Saline Agriculture, edited by: Jagdish Chander Dagar, Rajender Kumar Yadav, and Parbodh Chander Sharma. Published by Springer Nature Singapore Pte Ltd., 67-93, 2019.

Bannari, A., Al-Ali, Z. M.: Assessing Climate Change Impact on Soil Salinity Dynamics during the Last 30 years (1972-2017) in the Arid Landscape using Landsat TM, ETM+ and OLI data. Remote Sens., 12, 2794. doi:10.3390/rs12172794, 2020.

Bannari, A., Al-Ali, Z. M., and Kadhem, G.: Effects of Topographic Attributes and Water Table Depths on the Soil Salinity Accumulation in Arid Land. Proceedings of International Geoscience and Remote Sensing Symposium (IGARSS-2021), 12-14 July 2021, Brussels, Belgium, pp. 6548-6551, 2021.

Bannari, A., Asalhi, H., and Teillet, P. M.: Transformed Difference Vegetation Index (TDVI) for Vegetation Cover Mapping. Proceedings of International Geoscience and Remote Sensing Symposium (IGARSS'2002), Toronto, Ontario, 9-13 July. pp. 3053-3055. DOI: 10.1109/IGARSS.2002.1026867, 2002.

Bannari, A., El-Battay, Bannari, R., and Rhinane, H.: Sentinel-MSI VNIR and SWIR Bands Sensitivity Analysis for Soil Salinity Discrimination in an Arid Landscape. Remote Sens., 10(6), 855, 2018.

Bannari, A., El-Battay, A., Hameid, N., and Tashtoush, F.: Salt-Affected Soil Mapping in an Arid Environment using Semi-Empirical Model and Landsat-OLI Data. Adv. Remote Sensing, 6, 260–291, 2017b.

Bannari, A., Guedon, A. M., El-Harti, A., Cherkaoui, F. Z., and El-Ghmari, A.: Characterization of Slight and Moderate Saline and Sodic Soils in Irrigated Agricultural Land Using Simulated Data of ALI (EO-1) Sensor. Communications in Soil Science and Plant Analysis, 39, 2795-2811, 2008a.

Bannari, A., Guédon, A. M., and El-Ghmari, A.: Mapping Slight and Moderate Saline Soils in Irrigated Agricultural Land Using Advanced Land Imager Sensor (EO-1) Data and Semi-Empirical Models. Communications in Soil Science and Plant Analysis, 47, 1883-1906, 2016.

https://doi.org/10.5194/soil-2021-55
Preprint. Discussion started: 24 August 2021

Bannari, A., Hameid, N. Abuelgasim, A.A., and El-Battay, A.: Sentinel-MSI and Landsat-OLI Data Quality Characterization for High Temporal Frequency Monitoring of Soil Salinity Dynamic in an Arid Landscape. IEEE Journal of Selected Topics in Applied Earth Observations and Remote Sensing (IEEE-J-STARS), 13(1), 2434-2450, 2020.

Bannari, A., Huete, A. R., Morin, D., and Zagolski, F.: Effects of soil color and brightness on vegetation indices. Int. J. of Remote Sens., 17(10), 1885-1906, 1996.

Bannari, A., Khurshid, K. S., Staenz, K., and Schwarz, J.: A Comparison of Hyperspectral Chlorophyll Indices for Wheat Crop Chlorophyll Content Estimation Using Laboratory Reflectance Measurements. IEEE Transaction on Geosciences and Remote Sensing, 45(10), 3063-3073, 2007.

Bannari, A., Khurshid, S. K., Staenz, K., and Schwarz, J.: Potential of Hyperion EO-1 Hyperspectral Data for Wheat Crop Chlorophyll Content Extraction in Precision Agriculture. Canadian J. of Remote Sensing, 34(1), 139-157, 2008b.

Bannari, A., Morin, D., Huete, A. R., and Bonn, F.: A Review of Vegetation indices. Remote Sensing Reviews, 13, 95-120, 1995.

Bannari, A., Shahid, S. A., El-Battay, A., Alshankiti, A., Hameid, N. A., and Tashtoush, F.: Potential of WorldView-3 data for Soil Salinity Modeling and Mapping in Precision Agriculture Context. Proceedings of International Geoscience and Remote Sensing Symposium, IGARSS-17, 23-28 July 2017a, Texas, USA, pp. 1585-1588, 2017a.

Bannari, A., Staenz, K., Champagne, C., Khurshid, K. S. : Spatial variability mapping of crop residue using Hyperion (EO-1) hyperspectral data. Remote Sens., 7, 8107-8127, 2015.

Bannari. A., Teillet, P. M., and Richardson, G.: Nécessité de l'étalonnage radiométrique et standardisation des données de télédétection. Canadian J. of Remote Sensing, 25, 45-59, 1999.

Ben-Dor, E., Metternicht, M., Goldshleger, N., Mor, E., Mirlas, V., and Basson, U.: Review of Remote Sensing-Based Methods to Assess Soil Salinity. In: *Remote Sensing of Soil Salinization: Impact on Land Management*, edited by Metternicht, G. and Zinck, J.A., Eds.; CRC Press Taylor and Francis Group: Boca Raton, FL, USA, 39 - 60, 2009.

Ben-Dor, E., Ong, C., and Lau, I.C.: Reflectance measurements of soils in the laboratory: Standards and protocols. Geoderma, 245–246, 112–124, 2015.

Bharti, R., Kalimuthu,R., and Ramakrishnan, D.: Spectral Pathways for Exploration of Secondary Uranium: An Investigation in the Desertic Tracts of Rajasthan and Gujarat, India. Adv. in Space Research 56 (8), 1613–1626. doi:10.1016/j.asr.2015.07.015, 2015.

Boudibi, S., Sakaa, B., Benguega, Z., Fadlaoui, H., Othman, T., and Bouzidi, N.: Spatial prediction and modeling of soil salinity using simple cokriging, artificial neural networks, and support vector machines in El Outaya plain, Biskra, southeastern Algeria. Acta Geochim. (2021). https://doi.org/10.1007/s11631-020-00444-0, 2021.

Baret, F.: Contribution au suivi radiométrique de cultures de céréales. Thèse de Doctorat, Université Paris-Sud Orsay, France, 182pp, 1986.

https://doi.org/10.5194/soil-2021-55
Preprint. Discussion started: 24 August 2021

Bryant, R. G.: Validated linear mixture modelling of Landsat TM data for mapping evaporite minerals on a playa surface: methods and applications. Int. J. of Remote Sens., 17, 315–330, 1996.

Buck, B. J., King, J., and Etyemezian, V.: Effects of Salt Mineralogy on Dust Emissions, Salton Sea, California. Soil Sci. Soc. Am. J., 75, 1971–1985, 2011.

Burgess, D. W., Lewis, P., and Muller, J. P.: Topographic effects in AVHRR NDVI data. Remote Sens. of Environ., 54(3), 223-232, 1995.

Champagne, C., Bannari, A., Staenz, K., Deguise, J.-C., McNairn, H., and Shang, S.: Validation of a Hyperspectral Curve-Fitting Model for the Estimation of Plant Water Content of Agricultural Canopies. Remote Sens. of Environ., 87, 148-160, 2003.

Chéret, V., and Denux, J.-P.: Analysis of MODIS NDVI Time Series to Calculate Indicators of Mediterranean Forest Fire Susceptibility. GIScience and Remote Sensing, 48(2), 171-194. DOI: 10.2747/1548-1603.48.2.171, 2011.

Chivas, A. R.: Terrestrial Evaporites. Chapter 10 in Geochemical Sediments and Landscapes; Nash, D.J., McLaren, S.J., Eds.; RGS-IBG Book Series; Blackwell Pub.: Malden, MA, USA, 330–364, 2007.

Clark, R.N., and Roush, T. L.: Reflectance spectroscopy: Quantitative analysis techniques for remote sensing applications. J. of Geophysical Research, 89, 6329–6340, 1984.

Clark, R.N., and Swayze, G.A.: Mapping minerals, amorphous materials, environmental materials, vegetation, water, ice and snow, and other materials. The USGS Tricorder algorithm, *in* Green, R.O., ed., Summaries of the fifth annual NASA Jet Propulsion Laboratory airborne earth science workshop: Pasadena, NASA Jet Propulsion Laboratory Publication, 95(1), 39-40, 1995.

Clark, R. N., Gallagher, A. J., and Swayze, G. A.: Material absorption-band depth mapping of imaging spectrometer data using the complete band shape least-squares algorithm simultaneously fit to multiple spectral features from multiple materials. In: Proceedings of the Third Airborne Visible/Infrared Imaging Spectrometer (AVIRIS) Workshop, JPL Publication 90-54, pp. 176–186, 1990.

Clark, R. N., King, T. V. V., and Gorelick, N. S.: Automatic continuum analysis of reflectance spectra". In JPL Proceedings of the 3rd Airborne Imaging Spectrometer Data Analysis Workshop, 138-142, 1987. Available on line: https://ntrs.nasa.gov/archive/nasa/casi.ntrs.nasa.gov/19880004388.pdf (accessed on 18 March 2020).

Clark, R. N., Swayze, G. A., Livo, K. E., Kokaly, R. F., Sutley, S. J., Dalton, J. B., McDougal, R. R., and Gent, C. A., 2003. Imaging spectroscopy: earth and planetary remote sensing with the USGS Tetracorder and expert systems. J. of Geophysial. Research, 108(E-12), 5131. doi:10.1029/2002JE001847, pages 5-1 to 5-44.

Clark, R.N., Swayze, G.A., Carlson, R., Grundy, W., Noll, K.: Spectroscopy from Space. Reviews in Mineralogy and Geochemistry, 78(1), 399-446. doi:10.2138/rmg.2014.78.10, 2014.

Crowley, J.: Visible and near-infrared (0.4–2.5 mm) reflectance spectra of playa evaporate minerals. J. of Geochemical Research 96(B10), 16231–16240, 1991.

Crowley, J. K., Brickey, D. W., and Rowan, L. C.: Airborne imaging spectrometer data of the Ruby Mountains, Montana: mineral discrimination using relative absorption band-depth images. Remote Sens. Of Environ. 29(2), 121–134. https://doi.org/10.1016/0034-4257(89)90021-7, 1989.

https://doi.org/10.5194/soil-2021-55
Preprint. Discussion started: 24 August 2021

Csillag, F., Pasztor, L., and Biehl, L.: Spectral band selection for the characterization of salinity statues of soils. Remote Sens. of Environ., 43,231-42. doi:10.1016/0034-4257(93)90068-9, 1993.

Corwin, D., and Scudiero, E.: Review of soil salinity assessment for agriculture across multiple scales using proximal and/or remote sensors. Publications 2148 from USDA-ARS / UNL Faculty. https://digitalcommons.unl.edu/usdaarsfacpub/2148, 2019.

Dagar, J. C., Sharma, P. C., Chaudhari, S. K., Jat, H. S., and Ahamad, S.: Climate Change vis-a-vis Saline Agriculture: Impact and Adaptation Strategies. In: Innovative Saline Agriculture, edited by Dagar, J. C., Sharma, P. C., Sharma, D. K., and Singh, A. K., Springer India: Berlin, Germany, Volume 518, pp. 5–55, 2016.

Davis, E., Wang, C., and Dow, K.: Comparing Sentinel-2 MSI and Landsat-8 OLI in soil salinity detection: A case study of agricultural lands in coastal North Carolina. Int. J. of Remote Sens., *40*, 6134–6153. doi:10.1080/01431161.2019.1587205, 2019.

Dehaan, R. L., and Taylor, G. R.: Field-derived spectra of salinized soils and vegetation as indicators irrigation-induced soil salinization. Remote Sens. Environ., 80, 406-417, 2002.

Dehaan, R. L., and Taylor, G. R.: Image-derived spectral endmembers as indicators of salinization. Int. J. of Remote Sens., 24(4), 775-794, 2003.

El-Battay, A., Bannari, A., Hameid, N. A., and Abahussain, A. A.: Comparative Study among Different Semi-Empirical Models for Soil Salinity Prediction in an Arid Environment Using OLI. Adv. in Remote Sens., 6, 23-39, 2017.

Elhag, M.: Evaluation of different soil salinity mapping using remote sensing techniques in arid ecosystems Saudi Arabia. J. Sens., 101155/2016/7596175, 2016.

ENVI: Visual Information Solutions (*ENVI) Tutorial.* Boulder, Colorado, USA, 2012. Available online: http://www.exelisvis.com/docs/Tutorials.html (accessed on 26 May 2017), 2012.

Fan, X., Liu, Y., Tao, J., and Weng, Y.: Soil Salinity Retrieval from Advanced Multi-Spectral Sensor with Partial Least Square Regression. Remote Sens., 7, 488-511, 2015.

Fan, X., Pedroli, B., Liu, G., Liu, Q., Liu, H., and Shu, L.: Soil salinity development in the Yellow River Deltain relation to ground water dynamics. Land Degrad. Dev., 23(2), 175-189, 2012.

Fan, X., Weng, Y., and Tao, J.: Towards decadal soil salinity mapping using Landsat time series data. Int. J. of Appl.Earth Obs. and Geoinf., 52, 32-41, 2016.

FAO: Salt-affected soils. Accessed on 04-10-2018. http://www.fao.org/soils-portal/soil management/management-of-some-problem-soils/salt-affected-soils/more-information-on-salt-affected soils/en/, 2018.

Farifteh, J.: Imaging spectroscopy of salt-affected soils: Model-based integrated method. PhD Thesis (Dissertation 143), International Institute for Geo-information Science and Earth Observation (ITC), Enscheda, the Netherlands, 235 pp. 2007.

Farifteh, J., Farshad, A., and George, R.: Assessing salt-affected soils using remote sensing, solute modelling and geophysics. Geoderma 130, 191-206, 2006.

Farifteh, J., Van-Der-Meer, F., and Carranza, E. J. M.: Similarity measures for spectral discrimination of salt-affected soils. Int. J. of Remote Sens., 28(23), 5273-5293. DOI: 10.1080/01431160701227604, 2007.

https://doi.org/10.5194/soil-2021-55
Preprint. Discussion started: 24 August 2021

Farifteh, J., Van-der-Meer, F., Van-der-Meijde, M., and Atzberger, C.: Spectral characteristics of salt-affected soils: A laboratory experiment. Geoderma, 145(3-4), 196-206, 2008.

Ferdous, J., and Rahman, M.T.Ur.: Evaluating Different Salinity Indices for Soil Salinity Mapping of Coastal Region of Bangladesh. Proceedings of IEEE Region 10 Humanitarian Technology Conference (R10-HTC) 21 - 23 December, Dhaka, Bangladesh, 337-340, 2017.

Fernandez-Buces, N., Siebe, C., Cram, S., and Palacio, J.: Mapping Soil Salinity Using a Combined Spectral Response Index for Bare Soil and Vegetation: A Case Study in the Former Lake Texcoco, Mexico. J. of Arid Environ., 65(4), 644-667, 2006.

Fookes, P. G., and Lee, E. M.: The engineering geology of playas, salt playas and Salinas. Quarterly J. of Eng. Geology and Hydrog., 51, 287-298. https://doi.org/10.1144/qjegh2017-084, 2018.

Gao, B. C.: NDWI - a normalized difference water index for remote sensing of vegetation liquid water from space. Remote Sens. Environ. 58(3), 257–266. https://doi.org/10.1016/S0034-4257(96)00067-3, 1996.

Genderjahn, S., Alawi, M., Wagner, D., Schuller, I., Wanke, A., and Mangelsdorf, K.: Microbial community responses to modern environmental and past climatic conditions in omongwa pan, Western Kalahari: a paired 16S rRNA gene profiling and lipid biomarker approach. J. of Geophys. Res. Biogeo., 123, 1333–1351. doi:10.1002/2017JG004098, 2018.

Ghosh, G., Kumar, S., and Saha, S. K.: Hyperspectral Satellite Data in Mapping Salt-Affected Soils Using Linear Spectral Unmixing Analysis. J. of Indian Society of Remote Sens., 40, 129-136, 2012.

Gleeson, D. F., Pappalardo, R. T., Grasby, S. E., Anderson, M. S., Beauchamp, B., Castaño, R., Chien, S. A., Doggett, T., Mandrake, L., and Wagstaff, K. L.: Characterization of a sulfur-rich arctic spring site and field analog to europa using hyperspectral data. Remote Sens. Environ. 114(6), 1297-1311. https://doi.org/10.1016/j.rse.2010.01.011, 2010.

Golabkesh, F., Ghanavati, N., Nazarpour, A., and Nejad, T. B.: Monitoring Soil Salinity Changes, Comparison of Different Maps and Indices Extracted from Landsat Satellite Images (Case Study: Atabieh, Khuzestan). Pol. J. Environ. Stud., 30(2), 1-16. DOI:10.15244/pjoes/123503, 2021.

Gopalakrishnan, T., and Kumar, L.: Modeling and Mapping of Soil Salinity and its Impact on Paddy Lands in Jaffna Peninsula, Sri Lanka. Sustainability, 12, 8317, doi:10.3390/su12208317, 2020.

Gopalakrishnan, T., and Kumar, L.: Linking Long-Term Changes in Soil Salinity to Paddy Land Abandonment in Jaffna Peninsula, Sri Lanka. Agriculture, 11, 211. https://doi.org/10.3390/ agriculture11030211, 2021.

Hameid, N., and Bannari, A.: Relationship analysis between vegetation and rainfall in central Sudan using SPOT-VGT and climatic data. Int. J. of Remote Sens. Applications (IJRSA), 6, 30-40, 2016.

Hartemink A.: On the relation between soils and climate. Proceedings of the 20th World Congress of Soil Science, Jeju, South Korea, 8–13 June 2014. http://toc.proceedings.com/33662webtoc.pdf, 2014.

https://doi.org/10.5194/soil-2021-55
Preprint. Discussion started: 24 August 2021

Hassani, A., Azapagic, A., D'Odorico, P., Keshmiri, A., Shokri, N.: Desiccation crisis of saline lakes: A new decision-support framework for building resilience to climate change. Science of the Total Environment, 703 (2020) 134718, 2020.

Hoa, V. P., Giang, N. V., Binh, N. A., Hong-Hai, L. V., Pham, T. D., Hasanlou, M., and Bui, T. D.: Soil Salinity Mapping Using SAR Sentinel-1 Data and Advanced Machine Learning Algorithms: A Case Study at Ben Tre Province of the Mekong River Delta (Vietnam). Remote Sens. 11, 128. doi:10.3390/rs11020128, 2019.

Howari, F. M., Goodell, P. C., and Miyamoto, S.: Spectroscopy of Salts Common in Saline Soils. In R. S. Muttiah (Ed.), From Laboratory Spectroscopy to Remotely Sensed Spectra of Terrestrial Ecosystems, 1-20. https://doi.org/10.1007/978-94-017-1620-8_1, 2002a.

Howari, F. M., Goodell, P. C., and Miyamoto, S.: Spectral properties of salt crusts formed on saline soils. J. of Environmental Quality, 31(5), 1453-1461, 2002b.

Hu, J., Peng, J., Zhou, Y., Xu, D., Zhao, R., Jiang, Q., Fu, T., Wang, F., and Shi, Z.: Quantitative Estimation of Soil Salinity Using UAV-Borne Hyperspectral and Satellite Multispectral Images. Remote Sens., 11, 736. doi:10.3390/rs11070736, 2019.

Huang, S., Tang, L. Hupy, J. P., Wang, Y., Shao, G.: A commentary review on the use of normalized difference vegetation index (NDVI) in the era of popular remote sensing. J. For. Res. https://doi.org/10.1007/s11676-020-01155-1, 2020.

Huang, Z., Turner, B. J., Dury, S. J., Wallis, I. R., and Foley, W. J.: Estimating foliage nitrogen concentration from HYMAP data using continuum removal analysis. Remote Sens. of Environ. 93, 18–29, 2004.

Huete, A. R.: A soil-adjusted vegetation index (SAVI). Remote Sens. of Environ. 25:295-309, 1988.

Huete, A. R.: Soil influences in remotely sensed vegetation-canopy spectra. In: Theory and applications of optical remote sensing, edited by Asrar, G., New York: John Wiley & Sons, Inc., 107-141, 1989.

Huete, A. R., Didan, K., Miura, T., Rodriguez, E. P., Gao, X., and Ferreira, L. G.: Overview of the radiometric and biophysical performance of the MODIS vegetation indices. Remote Sens. Environ. 83(1), 195-213. http://dx.doi.org/10.1016/S0034-4257(02)00096-2, 2002.

Huete, A. R., HuiQing Liu, H., and Van-Leeuwen, W. J. D.: The Use of Vegetation Indices in Forested Regions: Issues of Linearity and Saturation. Proceedings of the International Geoscience and Remote Sensing Symposium (IGARSS-97), 1966-1968, 1997.

Huete, A. R., Justice, C., and Liu, H.: Development of Vegetation and Soil Indices for MODIS-EOS. Remote Sens. of Environ. 49, 224-234, 1994b.

Huete, A. R., Liu, H., De-Lira, G. R., Batchily, K., and Escadafal, R.: A soil color index to adjust for soil and litter noise in vegetation index imagery of arid regions. Proceedings of the International Geoscience and Remote Sensing Symposium (IGARSS-94), Pasadena, California, vol. II (Piscataway, NJ: LE.E.E.), 1042-1043, 1994a.

Hunt, G., and Salisbury, S.: Visible and near-infrared spectra of minerals and rocks. I. Silicate minerals. Modern Geology 1, 283–300, 1970.

Hunt, G., and Salisbury, J.: Visible and near-infrared spectra of minerals and rocks. II. Carbonates. Modern Geology 2, 23–30, 1971.

https://doi.org/10.5194/soil-2021-55
Preprint. Discussion started: 24 August 2021

Hunt, G., Salisbury, J., and Lenhoff, C.: Visible and near-infrared spectra of minerals and rocks. IV. Sulphides and sulfates. Modern Geology 3: 1–4, 1971.

IDNP: Indo-Dutch network project: A methodology for identification of waterlogging and soil salinity conditions using remote sensing, Karnal, India: Central Soil Salinity Research Institute, 78 pp., 2002.

Irons, J. R., Weismiller, R. A., and Petersen, W.: Soil reflectance. Chapter (66-106) in Theory and applications of optical remote sensing, edited by G. Asrar. New York: John Wiley & Sons, Inc., 66-106, 1989.

Ivushkin, K., Bartholomeus, H., Bregt, A. K., Pulatov, A., Kempen, B., and De-Sousa, L.: Global mapping of soil salinity change. Remote Sens. of Environ. 231(15), 111260.

Jackson, R. D., Slater, P. N. and Pinter, P. J.: Discrimination of growth and water stress in wheat by various vegetation indices through clear and turbid atmospheres. Remote Sens. of Environ. 13, 187-208, 1983.

Jackson, R. D, Pinter, P. J., Paul, J., Reginato, R. J., Robert, J., and Idso, S. B.: Hand-Held Radiometry. Agricultural Reviews and Manuals, ARM-W-19; U.S. Department of Agriculture Science and Education Administration: Phoenix, AZ, USA, 1980.

James, M. E., and Kalluri, S. N. V.: The Pathfinder AVHRR land data set: an improved coarse resolution data set for terrestrial monitoring. Int. J. Remote Sens. 15(17):3347–3363, 1994.

Jiang, H., Rusuli, Y., Amuti, T., and He, Q.: Quantitative assessment of soil salinity using multi-source remote sensing data based on the support vector machine and artificial neural network. Int. J. Remote Sens. 40, 284-306, 2019.

Joshi, D., Tóth, T., and Sári, D.: Visual discrimination of surface features of salt affected soils using satellite images in arid region of Rajasthan (India). J. Indian Soc. Remote Sens. 30, 33-38, 2002.

Katawatin, R., and Kotrapat, W.: Use of LANDSAT-7 ETM+ with ancillary data for soil salinity mapping in Northeast Thailand. In Microtechnologies for the New Millennium 2005. (ed.), Int. Society for Optics and Photonics, 708-716, 2005.

Kasim, N., Tiyip, T., Abliz, A., Nurmemet, I., Sawut, R., and Maihemuti, B.: Mapping and Modeling of Soil Salinity Using WorldView-2 Data and EM38-KM2 in an Arid Region of the Keriya River, China. Photogrammetric Engineering and Remote Sensing, 84(1), 43–52, 2018.

Kaufman, Y.J., and Holben, B.N.: Calibration of the AVHRR visible and near-IR bands by atmospheric scattering, ocean glint and desert reflection. Int. J. of Remote Sens. 14(1), 21-52, 1993.

Khurshid, K. S., Staenz, K., Bannari, A., Sun, L., Neville, R., White, H. P., Champagne, C. M., and Hitchcock, R.: Pre-processing of EO-1 Hyperion Data. Canadian J. of Remote Sens. 32(2), 84-97, 2006.

Khan, N. M., Rastoskuev, V. V., Shalina, E. V., and Sato, Y.: Mapping salt-affected soils using remote sensing indicators - A simple approach with the use of GIS IDRISI. Proceedings of the 22nd Asian Conference on Remote Sensing. Singapore, Center for Remote Imaging, Sensing and Processing (CRISP), National University of Singapore; Singapore Institute of Surveyors and Values; Asian Association on Remote Sensing, 2001.

Kinthada, N. R., Gurram, M. K., Eedara, A., and Velaga, V. R.: Remote Sensing and GIS in the Geomorphometric Analysis of Micro-Watersheds for Hydrological Scenario Assessment and Characterization: A Study on Sarada River Basin, Visakhapatnam District, India. Int. J. of Geomatics and Geosciences, 4, 195-212, 2013.

https://doi.org/10.5194/soil-2021-55
Preprint. Discussion started: 24 August 2021

Kokaly, R. F., Despain, D. G., Clark, R. N., and Livo, K. E.: Mapping vegetation in Yellowstone National Park using spectral feature analysis of AVIRIS data. Remote Sens. of Environ. 84, 437−456, 2003.

Kruse, F. A., Boardman, J. W., and Huntington, J. F.: Progress Report: Geologic Validation of EO-1 Hyperion. Proceedings of the 10th JPL Airborne Earth Science Workshop, Jet Propulsion Laboratory Publication, NASA, USA, 2001.

Labsphere: A guide to reflectance coatings and materials. Available at http://www.labsphere.com/tech_info/docs/Coating_&_Material_Guide.pdf, 2001.

Lasne, Y., Paillou, P., Freeman, A., Farr, T., McDonald, K., Ruffié, G., Malézieux, J.-M., and Chapman, B.: Study of Hyper-Saline Deposits and Analysis of their Signatures on Airborne and Spaceborne SAR Data: Example of Death Valley, California. IEEE Transactions on Geoscience and Remote Sensing 47(8), 2581-2598, 2009.

Leeuwen, W. J. D., Huete, A. R., and Laing, T. W.: MODIS Vegetation Index Compositing Approach: A Prototype with AVHRR Data. Remote Sens. of Environ. 69(3), 264-280, 1999.

Liu, H., Li, X., Mao, F., Zhang, M., Zhu, D., He, S., Huang, Z., and Du, H.: Spatiotemporal Evolution of Fractional Vegetation Cover and Its Response to Climate Change Based on MODIS Data in the Subtropical Region of China. Remote Sens. 13, 913. https://doi.org/10.3390/ rs13050913, 2021.

Lobell, D. B., Lesch, S. M., Corwin, D. L., Ulmer, M. G., Anderson, K. A., Potts, D. J., Doolittle, J. A., Matos, M. R., and Baltes, M. J.: Regional-scale assessment of soil salinity in the Red River Valley using multi-year MODIS EVI and NDVI. J. Environ. Qual., 39(1), 35–41, 2010.

Lowenstein, T. K., and Hardie, L. A.: Criteria for the recognition of salt-pan evaporites. Sedimentology, 32, 627–644, 1985.

Manchanda, M. L., and Khanna, S. S.: Use of aerial photograph for study of soil salinity and landscape relationship in parts of Haryana. J. Ind. Soc. Photo-Int. and Remote Sens. **7,** 27–34. https://doi.org/10.1007/BF02991453, 1979.

Manevski, K., Manakos, I., Petropoulos, G. P., and Kalaitzidis, C.: Discrimination of common Mediterranean plant species using field Spectroradiometry. Int. J. of Applied Earth Observation and Geoinformation, 13, 922–933, 2011.

Mashimbye, Z.E.: Remote Sensing of Salt-affected Soil. Ph.D. Thesis, Faculty of Agri-Sciences, Stellenbosch University, South Africa, 151 pp., 2013.

Masoud, A. A.: Predicting salt abundance in slightly saline soils from Landsat ETM+ imagery using Spectral Mixture Analysis and soil spectrometry. Geoderma, 217-218, 45-56, 2014.

Masoud, A. A., and Koike, K.: Arid land salinization detected by remotely-sensed land cover changes: a case study in the Siwa region, NW Egypt. J. of Arid Environ. 66(1), 151- 167, 2006.

Masoud, A. A., Koike, K., Atwia, M. G., El-Horiny, M. M., and Gemail, K. S.: Mapping soil salinity using spectral mixture analysis of landsat 8 OLI images to identify factors influencing salinization in an arid region. Int. J. Appl. Earth Obs. Geoinformation, 83(2019), 101944, 2019.

Mees, F.: Distribution patterns of gypsum and kalistrontite in a dry lake basin of the southwestern Kalahari (Omongwa pan, Namibia). Earth Surf. Process. Landf. 24, 731-744, 1999.

https://doi.org/10.5194/soil-2021-55
Preprint. Discussion started: 24 August 2021

Metternicht, G. I., and Zinck, J. A.: Spatial discrimination of salt- and sodium-affected soil surfaces. Int. J. of Remote Sens. 18, 2571-2586. doi:10.1080/014311697217486, 1997.

Metternicht, G. I., and Zinck, J. A.: Remote Sensing of Soil Salinity: Potentials and Constraints. Remote Sens. of Environ. 85, 1-20, 2003.

Metternicht, G., and Zinck, J.A.: Remote Sensing of Soil Salinization: Impact on Land Management. CRC Press Taylor and Francis Group, Boca Raton, FL, USA, 374 pp., 2009.

Milewski, R., Chabrillat, S., and Behling, R.: Analyses of Recent Sediment Surface Dynamic of a Namibian Kalahari Salt Pan Based on Multitemporal Landsat and Hyperspectral Hyperion Data. Remote Sens. 9, 170. https://doi.org/10.3390/rs9020170, 2017.

Milewski, R., Chabrillat, S., Brell, M., Schleicher, A. M., and Guanter, L.: Assessment of the 1.75 μm absorption feature for gypsum estimation using laboratory, air- and space-borne hyperspectral sensors. Int. J. of Applied Earth Observation and Geoinformation, 77, 69-83. https://doi.org/10.1016/j.jag.2018.12.012, 2019.

Milewski, R., Chabrillat, S., and Bookhagen, B.: Analyses of Namibian Seasonal Salt Pan Crust Dynamics and Climatic Drivers Using Landsat 8 Time-Series and Ground Data. Remote Sens. 12, 474. https://doi.org/10.3390/rs12030474, 2020.

Millington, A. C., Drake, N. A., Townshend, J. R. G., Quarmby, N. A., Settle, J. J., and Reading, A. J.: Monitoring salt playa dynamics using Thematic Mapper data. IEEE Transactions on Geoscience and Remote Sensing, 27, 754–761, 1989.

Milton, D.: Geology of the Arabian Peninsula, Kuwait, Geological Survey Professional Paper. Washington: United State Government Printing Office, 1967.

Mishra, N., Helder, D., Angal, A. Choi, J. and Xiong, X.: Absolute Calibration of Optical Satellite Sensors Using Libya 4 Pseudo Invariant Calibration Site. Remote Sens. 6, 1327-1346. Doi:10.3390/rs6021327, 2014.

Moore, I. D., Gessier, P. E., Nielsen, G. A., Peterson, G. A.: Soil Attribute Prediction Using Terrain Analysis. Soil Sc. Society American J. 57, 443-452, 1993.

Mougenot, B., Pouget, M., and Epema, G.: Remote sensing of salt affected soils. Remote sensing review, 7, 241-259, 1994.

Mougenot, B., Pouget, M., and Epema, G.: Remote sensing of salt affected soils. Remote Sensing Reviews 7:241–259. Doi:10.1080/02757259309532180, 1993.

Mulder, V. L., De-Bruin, S., Schaepman, M. E., and Mayr, T. R.: The use of remote sensing in soil and terrain mapping: a review. Geoderma, 162(1–2), 1–19. https://doi.org/10.1016/j.geoderma.2010.12.018, 2011.

Myneni, R. B., and Asrar, G.: Atmospheric effects and spectral vegetation indices. Remote Sens. of Environ. 47, 390–402. doi:10.1016/0034-4257(94)90106-6, 1994.

Naing-OO, A., Iwai, C. B., and Saenjan, P.: Food Security and Socio-economic Impacts of Soil Salinization in Northeast Thailand. Int. J. of Environmental and Rural Development, 4(2), 76-81, 2013.

Nawar, S., Buddenbaum, H., and Hill, J.: Digital Mapping of Soil Properties Using Multivariate Statistical Analysis and ASTER Data in an Arid Region. Remote Sens. 7(2), 1181–1205, 2015.

https://doi.org/10.5194/soil-2021-55
Preprint. Discussion started: 24 August 2021

Nawar, S., Buddenbaum, H., Hill, J., and Kozak, J.: Modeling and Mapping of Soil Salinity with Reflectance Spectroscopy and Landsat Data Using Two Quantitative Methods (PLSR and MARS). Remote Sens. 6(11), 10813–10834, 2014.

Neto, O. C., Teixeira, A., Leão, R. A. O., Moreira, L. C. J., and Galvão, L. S.: Hyperspectral Remote Sensing for Detecting Soil Salinization Using ProSpecTIR-VS Aerial Imagery and Sensor Simulation. Remote Sens. 9, 42. doi:10.3390/rs9010042, 2017.

Nguyen, K. A., Liou, Y. A., Tran, H. P., Hoang, P.-P., and Nguyen, T.-H.: Soil salinity assessment by using near-infrared channel and Vegetation Soil Salinity Index derived from Landsat 8 OLI data: a case study in the Tra Vinh Province, Mekong Delta, Vietnam. Progress in Earth Planetary Sci. 7, 1(2020). https://doi.org/10.1186/s40645-019-0311-0, 2020.

Norman, C. P.: Kyvalley [Victoria] EM38 Salinity Survey. Research Report Series, Department of Agriculture and Rural Affairs, Victoria. Available online: http://agris.fao.org/agris-search/search.do?recordID¼AU9430080 (Accessed in February, 2020), 1989.

Nurmemet, I., Sagan, V., Ding, J.-L., Halik, Ü., Abliz, A., and Yakup, Z.: A WFS-SVM Model for Soil Salinity Mapping in Keriya Oasis, Northwestern China Using Polarimetric Decomposition and Fully PolSAR Data. Remote Sens. 10, 598. doi:10.3390/rs10040598, 2018.

Omar, S., and Shahid, S. A.: Reconnaissance Soil Survey for the State of Kuwait. In: Developments in Soil Classification, Land Use Planning and Policy Implications: Innovative Thinking of Soil Inventory for Land Use Planning and Management of Land Resources, edited by Shahid, S. A., Taha, F. K. and Abdelfattah, M. A., Springer Science and Business Media, Dordrecht, 85-107, 2013.

Owen, A. J.: Uses of Derivative Spectroscopy. Application Note, Agilent Technologies Innovating the HP Way, 1995. Available online: http://www.whoi.edu/cms/files/derivative_spectroscopy_59633940_175744.pdf (accessed on 2 February 2020), 1995

Pacheco, A., Bannari, A., Staenz, K., McNairn, H.: Deriving Percent Crop Cover over Agriculture Canopies Using Hyperspectral Remote Sensing. Canadian J. of Remote Sensing, special issue for hyperspectral remote sensing, 34(1), 110-123, 2008.

Pahlevan, N., Lee, Z.,Wei, J., Schaaf, C., Schott, J. R., and Berk, A.: On-orbit radiometric characterization of OLI (Landsat-8) for applications in aquatic remote sensing. Remote Sens. of Environ. 154, 272–284, 2014.

PCI-Geomatica: Using PCI Software. Richmond Hill, Ontario, Canada, 540 pp., 2018.

Peng, J., Biswas, A., Jiang, Q. S., Zhao, R. Y., Hu, J., Hu, B. F., and Shi, Z.: Estimating soil salinity from remote sensing and terrain data in southern xinjiang province, china. Geoderma, 337, 1309–1319, 2019.

Peon, J., Recondo, C., Fernandez, S., Calleja, J. F., De-Miguel, E., and Carretero, L.: Prediction of topsoil organic carbon using airborne and satellite hyperspectral imagery. Remote Sens. 9 (12), https://doi.org/10.3390/rs9121211, 2017.

Price, J.C.: Radiometric calibration of satellite sensors in the visible and near infrared. History and Outlook, Remote Sens. of Environ. 22, 3-9. doi:10.1016/0034-4257(87)90025-3, 1987.

https://doi.org/10.5194/soil-2021-55
Preprint. Discussion started: 24 August 2021

Rao, B. R., Dwivedi, R. S., Venkataratnam, L., Ravishankar, T., Thammappa, S. S., Bhargawa, G. P., and Singh, A.N.: Mapping the magnitude of sodicity in part of the Indo-Gangetic plains of Uttar Pradesh, Northern India using Landsat-TM. Int. J. of Remote Sens. 12, 419-25. doi:10.1080/01431169108929662, 1991.

Reynolds, R. L., Yount, J. C., Reheis, M., Goldstein, H., Chavez, P., Fulton, R., Whitney, J., Fuller, C., and Forester, R. M.: Dust emission from wet and dry playas in the Mojave Desert, USA. Earth Surf. Process. Landf., 32, 1811-1827, 2007.

Richards, L. A.: Diagnosis and improvement of saline and alkali soils. U.S. Salinity Laboratory DA, US Department of Agriculture Handbook No. 60, 166 pp., 1954.

Rouse, J. W., Haas, R. W., Schell, J. A., Deering, D. W., and Harlan, J. C.: Monitoring the vernal advancement and retrogradation (Greenwave effect) of natural vegetatioa NASA/GSFCT Type III Final Report, Greenbelt, MD, USA, 1974.

Running, S. W., Justice, C. O., Salmonson, V., Hall, D., Barker, J., and Kaufmann, Y. J.: Terrestrial remote sensing science and algorithms planned for EOS/MODIS. Int. J. Remote Sens. 15, 3587-3620, 1994.

Sandmeier, St., Muller, Ch., Hosgood, B., and Andreoli, G.: Sensitivity Analysis and quality Assessment of Laboratory BRDF Data. Remote Sens. of Environ. 64, 176-191, 1998.

Schuller, I., Belz, L., Wilkes, H., and Wehrmann, A.: Late Quaternary shift in southern African rainfall zones: Sedimentary and geochemical data from Kalahari pans. Zeitschrift Für Geomorphologie, 61(4), 339–362, 2018.

Shahid, S. A., and Behnassi, M.: Climate Change Impacts in the Arab Region: Review of Adaptation and Mitigation Potential and Practices. In: Vulnerability of Agriculture, Water and Fisheries to Climate Change: Toward Sustainable Adaptation Strategies, edited by Behnassi, M., Muteng'e, M. S., Ramachandran, G., and Shelat, K. N., Springer, Berlin, Germany, 15-58, 2014.

Shahid, S.A., and Rahman, K.: Soil salinity development, classification, assessment and management in irrigated agriculture. In: Handbook of Plant and Crop Stress (3rd edition), edited by Pessarakli, M., Taylor and Francis Group, Abingdon, Oxfordshire, UK, 23-39, 2011.

Shahid, S. A., Abdelfattah, M. A., Omar, S., Harahsheh, H., Othman, Y., abd Mahmoudi, H.: Mapping and monitoring of soil salinization in remote sensing, GIS, electro-magnetic induction and conventional methods – case studies. Proceedings of Int. Conf. of Soil Salinization and Groundwater Salinization in Arid Regions, Sultan Qaboos University, Muscat (Oman), 11-14 Jan., Volume 1, 59-97, 2010.

Shahid, S. A., Zaman, M., and Heng, L. L.: Soil Salinity: Historical Perspectives and a World Overview of the Problem. In: Guideline for Salinity Assessment, Mitigation and Adaptation Using Nuclear and Related Techniques, edited by Zaman, M., Springer Nature (AG), Basel, Switzerland, 43-53, 2018.

Shamsi, S. R. F., Zare, S., and Abtahi, S. A.: Soil salinity characteristics using moderate resolution imaging spectroradiometer (MODIS) images and statistical analysis. Arch. Agron. Soil Sci. 59, 471-489. doi:10.1080/03650340.2011.646996, 2013.

Shaw, P. A., and Bryant, R. G.: Pans, Playas and Salt Lakes. In: Arid Zone Geomorphology: Process, Form and Change in Dry lands (3rd Edition), edited by David, S. G. Thomas, Published by John Wiley & Sons, Ltd. DOI:10.1002/9780470710777, 373-401, 2011.

https://doi.org/10.5194/soil-2021-55
Preprint. Discussion started: 24 August 2021

Sidike, A., Zhao, S., and Wen, Y.: Estimating soil salinity in Pingluo County of China using QuickBird data and soil reflectance spectra. Int. J. Appl. Earth Obs. Geoinf. 26, 156-175, 2014.

Soil Science Division Staff: Soil Survey Manual. United States Department of Agriculture Handbook No. 18, 2017.

Steven, M. D., Malthus, T. J., Baret, F., Xu, H., and Chopping, M. J.: Inter-calibration of vegetation indices from different sensor systems. Remote Sens. of Environ. 88, 412-422, 2003.

Sumner, M. E., Miller, W. P., Kookana, R. S., and Hazelton, P.: Sodicity, dispersion, and environmental quality. In: Sodic soils: Distribution, properties, management, and environmental Consequences, edited by Sumner, M. E. and Naidu, R., New York: Oxford University Press, 149-172, 1998.

Taghadosi, M. M., Hasanlou, M., Eftekhari, K.: Retrieval of soil salinity from Sentinel-2 multispectral imagery. European J. of Remote Sens. 52(1), 138-154. DOI: 10.1080/22797254.2019.1571870, 2019.

Teh, S., and Koh, H.: Climate Change and Soil Salinization: Impact on Agriculture, Water and Food Security. Int. J. Agric. For. Plant. *2*, 1–9, 2016.

Teillet, P.M., and Santer, R.: Terrain Elevation and Sensor Altitude Dependence in a Semi-Analytical Atmospheric Code". Canadian J. of Remote Sens. 17, 36-44, 1991.

Teillet, P.M., Staenz, K., and Williams, D.J. Effects of spectral and spatial resolution on NDVI. Canada Centre for Remote Sensing, Ottawa, Ontario, Canada, 10 pp., 1994.

Teillet, P.M., Staenz, K., and Williams, D.J.: Effects of Spectral, Spatial, and Radiometric Characteristics on Remote Sensing Vegetation Indices of Forested Regions. Remote Sens. of Environ. 61, 139-149, 1997.

Thenkabail, P. S., Enclona, E. A., Ashton, M. S., and Van-Der-Meer, B.: Accuracy assessments of hyperspectral waveband performance for vegetation analysis applications. Remote Sens. of Environ. 91, 354-376, 2004.

Thenkabail, P. S., Lyon, J. G., Huete A. R.: Advanced Applications in Remote Sensing of Agricultural Crops And Natural Vegetation. In Hyperspectral Remote Sensing of Vegetation, 2nd Edition. CRC Press, 425 pp., 2018.

USDA: Soil Taxonomy: A basic System of Soil Classification for making and Interpreting Soil Surveys. USA: United States Department of Agriculture, 1999.

USDA: Soil Survey Laboratory Methods Manual; Soil Survey Investigations Report, No. 42 Version 4; Burt, R., Ed.; USDA-NRCS, Washington, DC, USA, 736 pages, 2004.

USDA: Kellogg Soil Survey Laboratory Methods Manual. Soil Survey Investigations Report No. 42, Version 5.0; Burt, R., Staff, S.S., Eds.; U.S. Department of Agriculture, Natural Resources Conservation Service, Washington, DC, USA, 2014.

Van-Der-Meera, F.: Analysis of spectral absorption features in hyperspectral imagery. Int. J. Appl. Earth Observation and Geoinformation, 5, 55–68, 2004.

Verma, K. S., Saxena, R. K., Barthwal, A. K., and Deshmukh, S. N.: Remote sensing technique for mapping salt affected soils. Int. J. of Remote Sens. 15(9), 1901-1914, 1994.

Wang, J., Peng, J., Li, H., Yin, C., Liu, W., Wang, T., and Zhang, H.: Soil Salinity Mapping Using Machine Learning Algorithms with the Sentinel-2 MSI in Arid Areas, China. Remote Sens. 13, 305, https://doi.org/10.3390/rs13020305, 2021.

https://doi.org/10.5194/soil-2021-55
Preprint. Discussion started: 24 August 2021

Wang, J., Ding, J., Yu, D., Teng, D., He, B., Chen, X., Ge, X., Zhang, Z., Wang, Y., Yang, X., Shi, T., and Su, F.: Machine learning-based detection of soil salinity in an arid desert region, Northwest China: A comparison between Landsat-8 OLI and Sentinel-2 MSI. Science of the Total Environment, 707, 136092, https://doi.org/10.1016/j.scitotenv.2019.136092, 2020.

Wang, J., Ding, J., Abulimiti, A., and Cai, L.: Quantitative estimation of soil salinity by means of different modeling methods and visible-near infrared (VIS-NIR) spectroscopy, Ebinur Lake Wetland, Northwest China. Peer J 6:e4703; DOI 10.7717/peerj.4703, 2018.

Wang, X., Hua, T., Zhang, C., Lang, L., and Wang, H.: Aeolian salts in Gobi deserts of the western region of Inner Mongolia: Gone with the dust aerosols. Atmos. Res. *118*, 1-9. doi:10.1016/j.atmosres.2012.06.003., 2012.

Wei, G., Li, Y., Zhang, Z., Chen, Y., Chen, J., Yao, Z., Lao, C., and Chen, H.: Estimation of soil salt content by combining UAV-borne multispectral sensor and machine learning algorithms. PeerJ 8:e9087; DOI 10.7717/peerj.9087, 2020.

Weng, Y., Gong, P., and Zhu, Z.: Soil salt content estimation in the Yellow Riverdelta with satellite hyperspectral data. Canadian J. of Remote Sens. 34 (3), 259–270, 2008.

Whitney, K., Scudierob, E., El-Askary, H. M., Skaggs, T. H., Allali, M., and Corwin, D. L.: Validating the use of MODIS time series for salinity assessment over agricultural soils in California, USA. Ecological Indicators 93 (2018) 889–898, 2018.

Wu, W., Zucca, C., Muhaimeed, A. S., Al-Shafie, W. M., Fadhil, A. M., Al-Quraishi, A. M. F, Nangia, V., Zhu, M., and Liu, G.: Soil salinity prediction and mapping by machine learning regression in Central Mesopotamia, Iraq. Land Degrad Dev. 29, 4005-4014, 2018.

Wu, W., Al-Shafie, W. M., Mhaimeed, A. S., Ziadat, F., Nangia, V., and Payne, W. B.: Soil Salinity Mapping by Multiscale Remote Sensing in Mesopotamia, Iraq. IEEE J. of Sel. Topics in Applied E.O. and Remote Sens. 7(11), 4442-4452, 2014.

Xenarios, S., Schmidt-Vogt, D., Qadir, M., Janusz-Pawleta, B., and Abdullaev, I.: The Aral Sea Basin.Water for Sustainable Development in Central Asia. Rout ledge Taylors & Francis Group London and New York, 2020.

Zhu, B., and Yang, X.: The Origion and Distribution of Soluble Salts in the Sand Seas of Nortern China. Geomorphology, 123, 232–242, 2010.

Zhu, K., Sun, Z., Zhao, F., Yang, T., Tian, Z., Lai, J., Zhu, W., and Long, B.: Relating Hyperspectral Vegetation Indices with Soil Salinity at Different Depths for the Diagnosis of Winter Wheat Salt Stress. Remote Sens. 13, 250. https://doi.org/10.3390/rs13020250, 2021.

Zhang, H. K., and Roy, D. P.: Computationally inexpensive Landsat 8 operational land imager (OLI) pan-sharpening. Remote Sens. 8(3), 180, 2016.

Zhang, H .K., Schroder, J. L., Pittman, J. J., Wang, J. J., and Payton, M. E.: Soil Salinity Using Saturated Paste and 1:1 Soil to Water Extracts. Soil Sci. Soc. Am. J., 69, 1146–1151, 2005.

Zhang, T. T., Zeng, S. L., Gao, Y., Ouyang, Z. T., Li, B., Fang, C. M., and Zhao, B.: Using hyperspectral vegetation indices as a proxy to monitor soil salinity. Ecol. Indic., 11, 1552–1562, 2011.

https://doi.org/10.5194/soil-2021-55
Preprint. Discussion started: 24 August 2021

Zinck, J.A., and Metternicht, G.: Soil Salinity and Salinization Hazard. In: Remote Sensing of Soil Salinization: Impact on Land Management, edited by Metternicht, G. and Zinck, J. A., CRC Press Taylor and Francis Group: Boca Raton, FL, USA, 3-20, 2009.

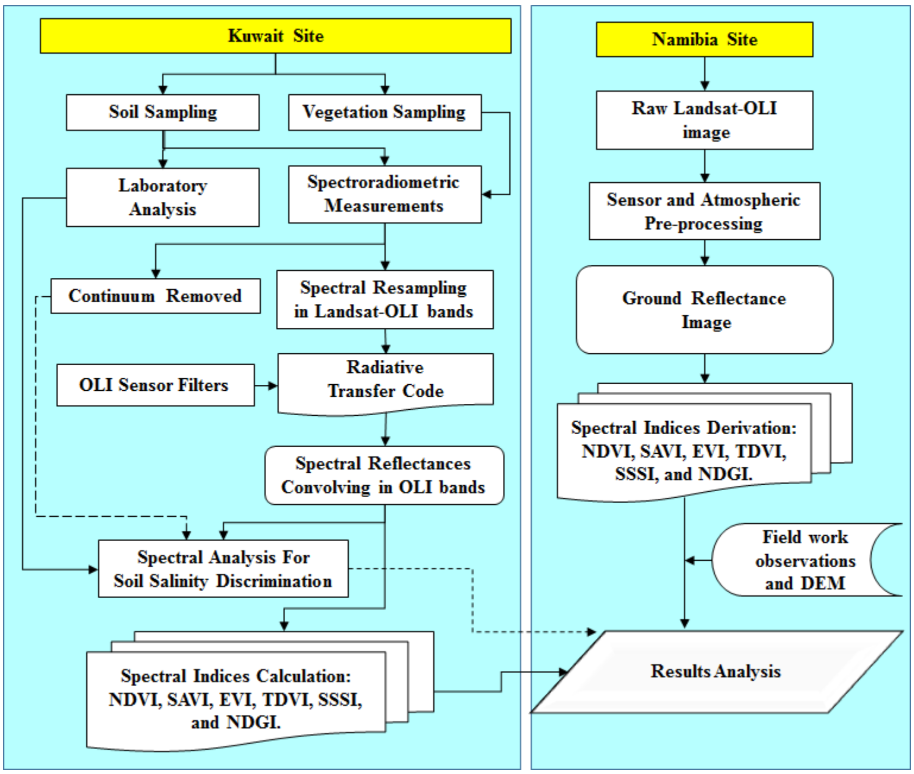

Figure 1: Methodology Flowchart.

https://doi.org/10.5194/soil-2021-55
Preprint. Discussion started: 24 August 2021

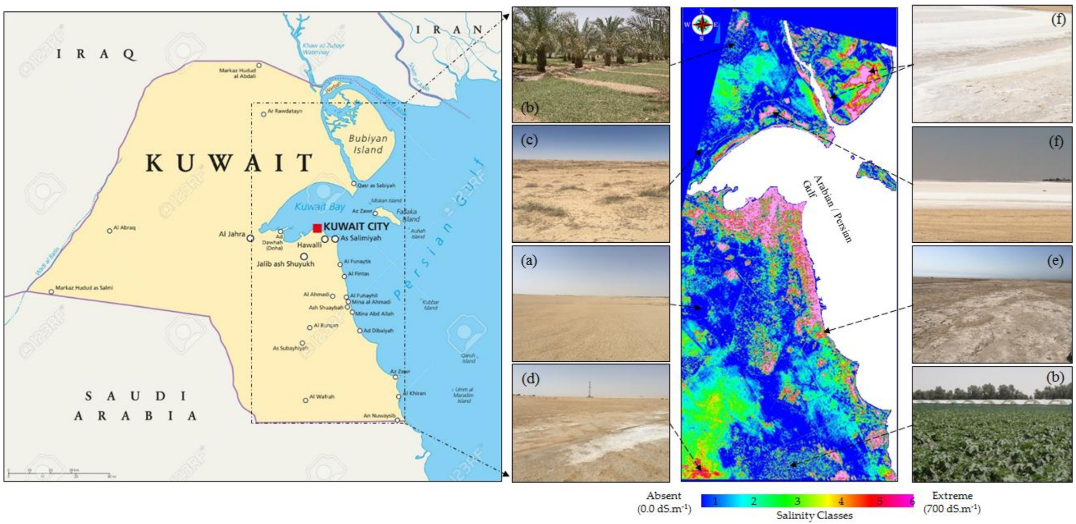

Figure 2: Maps of Kuwait study site location and soil salinity with photos illustrating salinity classes (Maps and photos from: Bannari and Al-Ali, 2020).

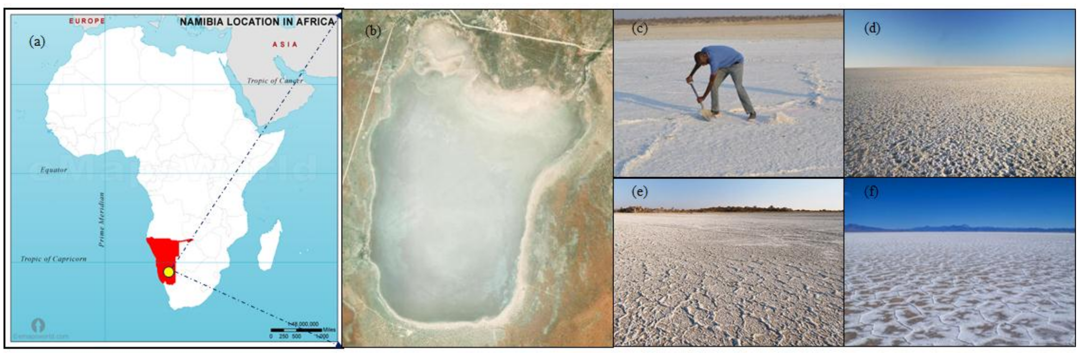

Figure 3. Location map of Omongwa salt playa site in Namibia in Africa (a, from Esri), Landsat-OLI RGB image (b), and photos (c-f) illustrating the accumulation of salt crust (source: https://www.namibiansun.com/news/gecko-denies-legal-threat2017-12-01).

https://doi.org/10.5194/soil-2021-55
Preprint. Discussion started: 24 August 2021

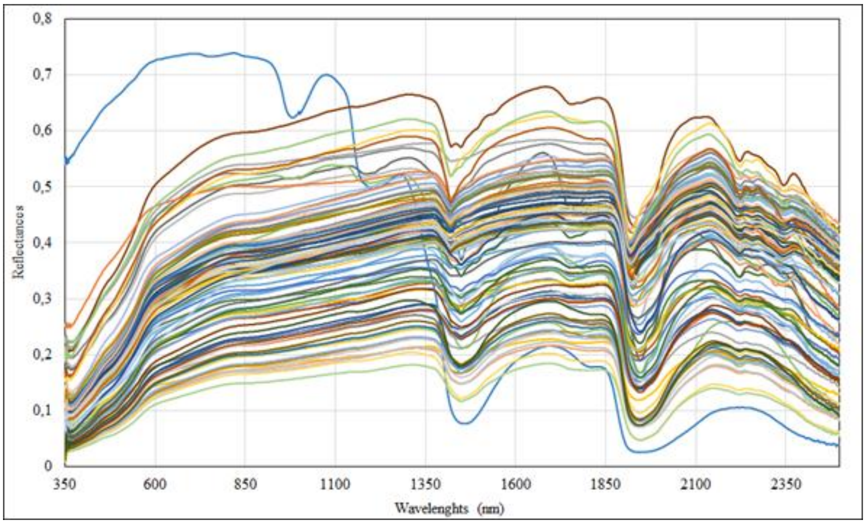

Figure 4. Spectral signatures of 100 soil samples with different degrees of salinity.

https://doi.org/10.5194/soil-2021-55
Preprint. Discussion started: 24 August 2021

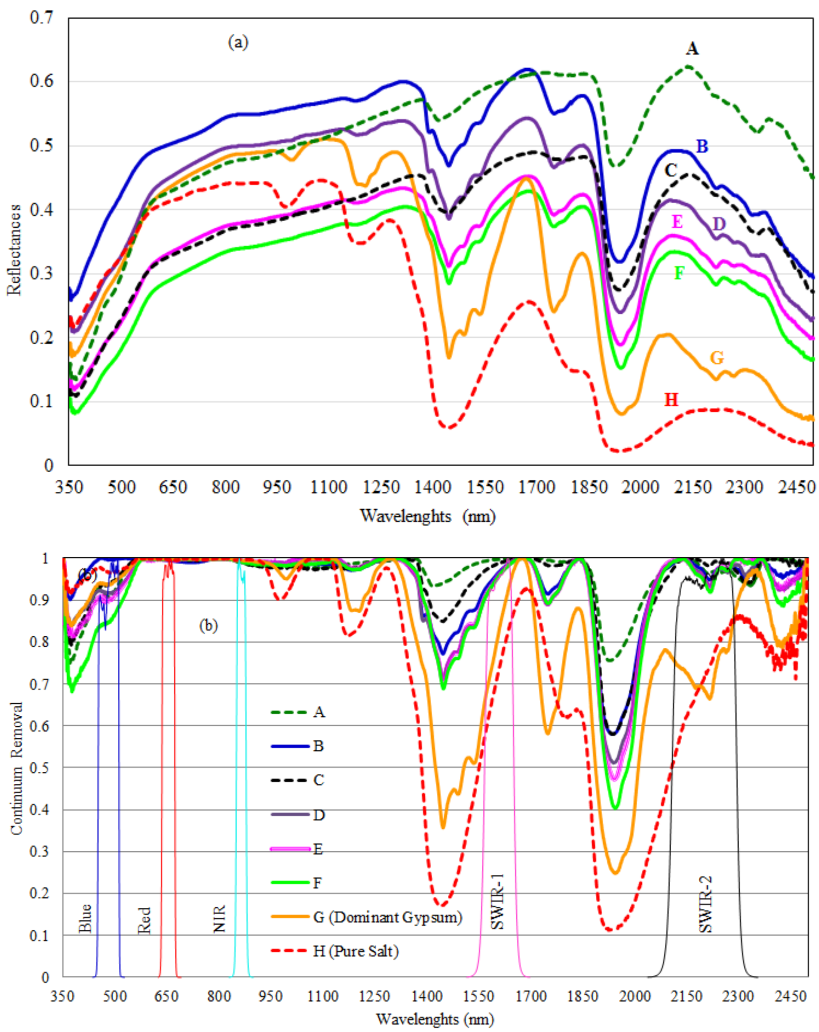

Figure 5. Spectral signatures of some soil samples with different salt contents (a) and their continuum removal with OLI filters profiles in blue, red, NIR and SWIR bands (b).

https://doi.org/10.5194/soil-2021-55
Preprint. Discussion started: 24 August 2021

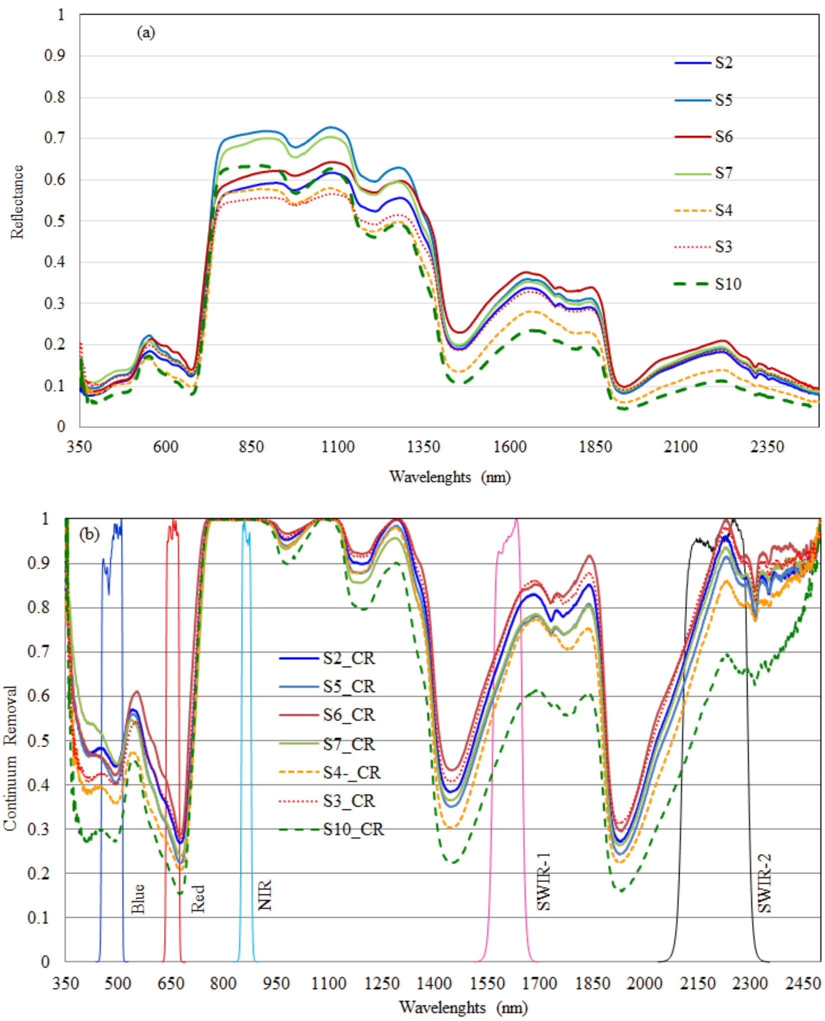

Figure 6. Spectral signatures of vegetation cover with different LAI (a) and their continuum removal with OLI filters profiles in blue, red, NIR and SWIR bands (b).

https://doi.org/10.5194/soil-2021-55
Preprint. Discussion started: 24 August 2021

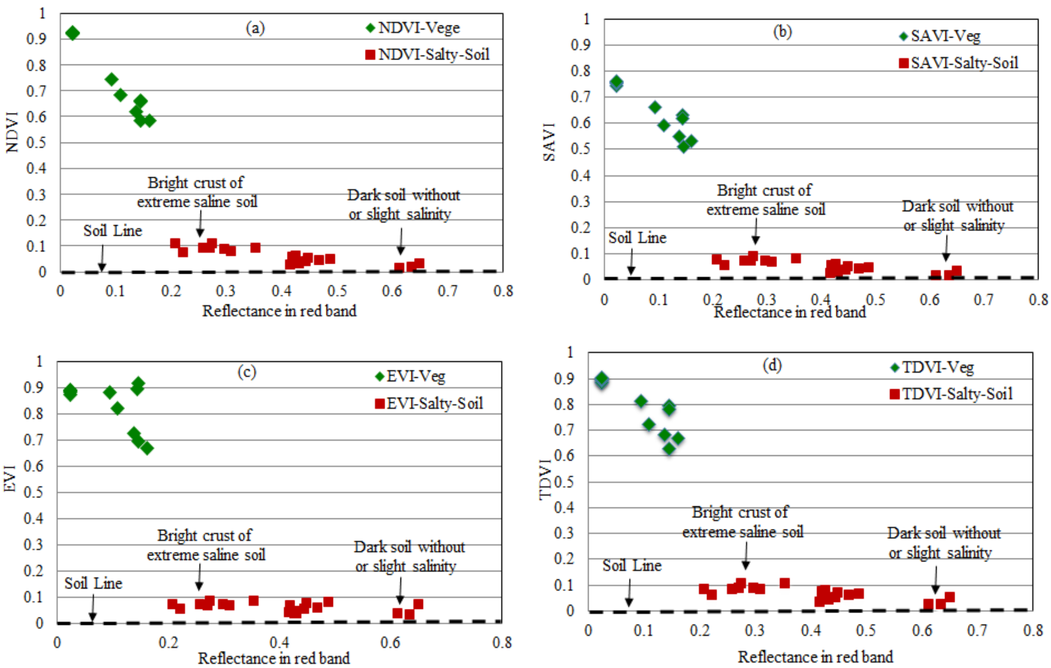

Figure 7. Sensitivity of VI's to discriminate soil salinity contents and LAI rates.

https://doi.org/10.5194/soil-2021-55
Preprint. Discussion started: 24 August 2021

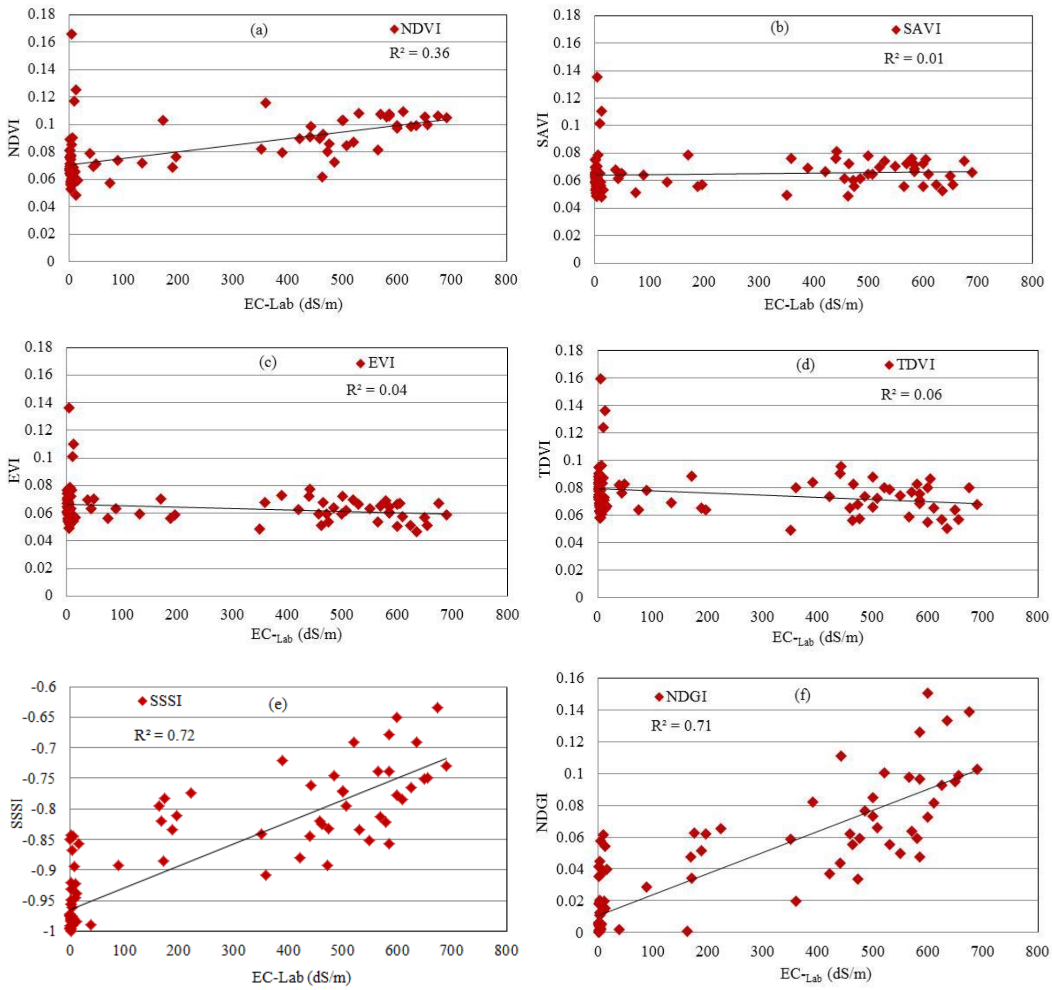

Figure 8. Statistical fits between the considered VI's and EC-$_{\text{Lab}}$.

https://doi.org/10.5194/soil-2021-55
Preprint. Discussion started: 24 August 2021

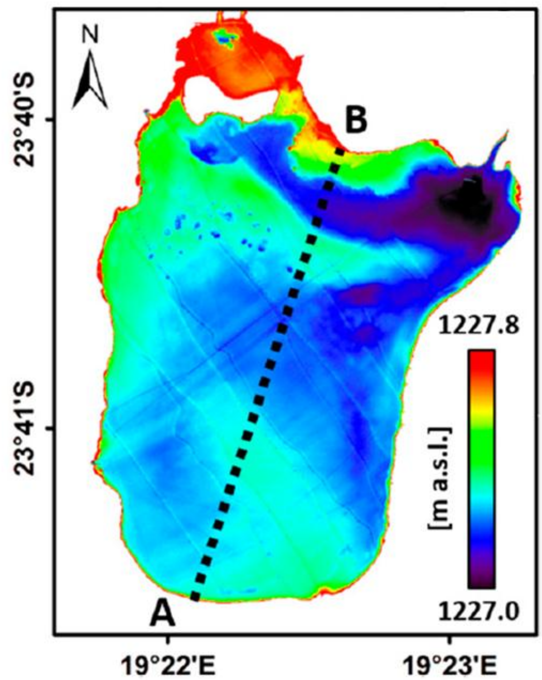

1392

1393 **Figure 9.** Lidar DEM characterizing the topographic variability across the pan site (Milewski et al., 2017).

1394

https://doi.org/10.5194/soil-2021-55
Preprint. Discussion started: 24 August 2021

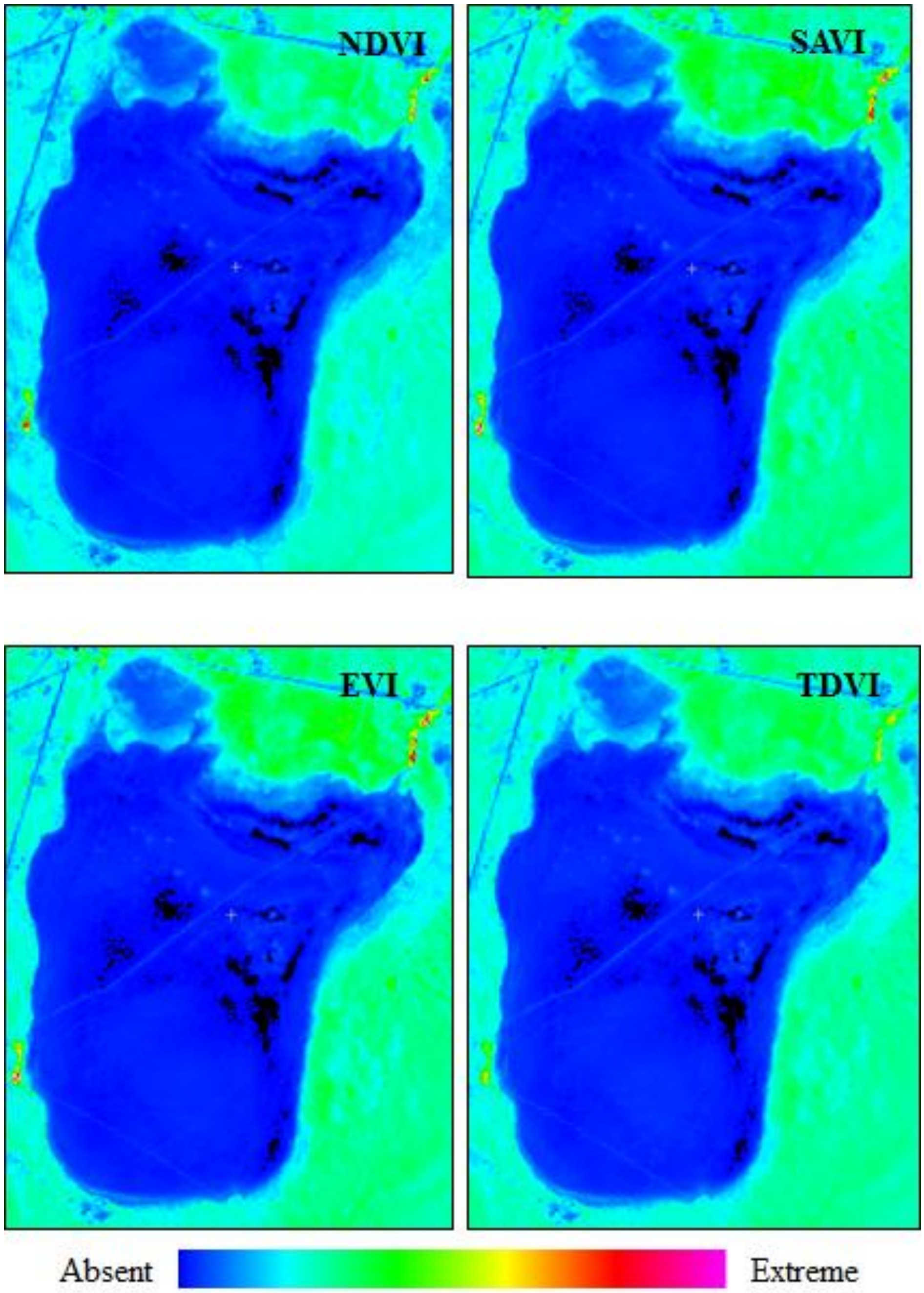

1395

1396 **Figure 10.** Assumed soil salinity maps derived based on VI's.

1397

https://doi.org/10.5194/soil-2021-55
Preprint. Discussion started: 24 August 2021

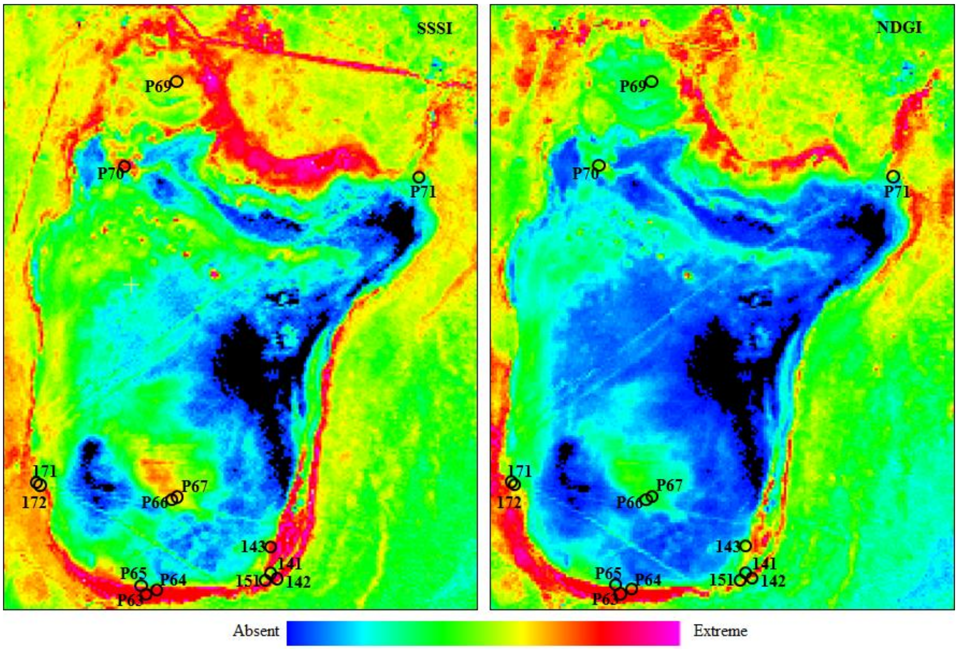

Figure 11. Soil salinity maps derived by evaporite mineral indices: SSSI and NDGI.

https://doi.org/10.5194/soil-2021-55
Preprint. Discussion started: 24 August 2021

Table 1. Description of some considered soil samples.

Sample Number	Sample Name	Munsell Color	EC (dS.m^{-1})	pHs	SAR (mmoles/L)$^{0.5}$	Texture	Description
1	K-19	7.5 YR	18.2	6.77	30.20	Sandy	Sandy soil without gypsum and shells
2	K-84	10 YR	635.0	6.24	449.50	Sandy-Clay-Loam	Crust of salt with small amount of gypsum
3	K-88	10 YR	583.0	6.46	468.10	Sandy-Clay-Loam	Crust of salt with small amount of gypsum
4	S-10-1	10YR 7/2	247.5	8.85	309.26	Sandy-Loam	Dominant salt crust with gypsum crystals
5	S-41-1	10YR 8/1	506.9	6.90	425.00	Pure salt (halit)	Salt scald-Sabkha
6	S-49-2	10YR 7/3	108.6	7.70	256.00	Sandy	Sandy saline soil without gypsum
7	Ba-33-B	18YR 8/1	7.3	8.16	57.79	Loamy-Sandy	Sandy soil with slight salinity, agricultural farm
8	Ba-33-C	5Y 8/1	5.5	8.39	55.13	Loamy-Sandy	Sandy soil with slight salinity, agricultural farm
9	Ba-15-C	10YR 8/1	399.0	7.71	298.85	Sandy-Loam	Pure gypsum crystal deposited by wind erosion
10	Ba-16-C	10YR 7/1	388.0	7.61	403.56	Sandy-Loam	Gypsum rocks at the surface
11	Pure-salt-Dry	10YR 8/1	509.0	7.50	465.00	Pure salt (halite)	Salt scald-Sabkha
12	Pure-Salt-Wet	10YR 8.1	512.0	7.10	389.00	Pure salt (halite)	Salt scald-Sabkha
13	A	10YR 7/6	2.4	7.7	1.60	Sandy	Sandy soil without gypsum and shells
14	B	10YR 8/1	55.6	8.10	84.50	Sandy-Clay-Loam	With small amount of gypsum crystals and shells
15	C	10YR 7/2	119.6	7.71	162.00	Loamy-Sandy	Sandy soil with small amount of gypsum crystals and shells
16	D	10YR 7/2	195.3	7.47	225.90	Sandy-Loam	Beginning of salt crust formation. Small amount of gypsum crystals and shells
17	E	10YR 7/2	333.0	7.57	325.20	Sandy-Clay-Loam	Beginning of salt crust formation. Small amount of gypsum crystals and shells
18	F	10YR 7/2	406.5	7.35	403.60	Sandy-Clay-Loam	Crust of salt with gypsum, calcium carbonate, and small amount of shells
19	G	5Y 8/1	445.5	7.60	415.20	Sandy	Mixture of pure gypsum crystal and salt deposited by wind erosion
20	H	10YR 8/1	507.0	7.60	444.70	Pure salt (halite)	Salt scald-Sabkha

https://doi.org/10.5194/soil-2021-55
Preprint. Discussion started: 24 August 2021

1426 **Table 2.** Laboratory analyses of Omongwa soil surface samples (locations in Fig. 11).

Point Number	EC_{-Lab} ($dS.m^{-1}$)	pHs	Mineralogy analysis (in %) Halite	Gypsum	Quartz	Calcite	Sepiolite	Soil
P63	17.6	8.6	5	75	19	0	0	Sandy
P64	17.6	8.6	36	47	17	-	-	-
P65	42.3	8.5	14	83	3	-	-	-
P66	42.3	8.5	41	44	13	-	1	-
P67	80.7	8.4	46	45	3	-	5	Sandy and Silty
P69	36.5	8.7	15	0	28	41	15	-
P70	33.7	8.6	16	27	32	15	11	-
P71	33.7	8.6	7	0	26	47	6	-
141	33.7	8.6	94	3	1	0	0	-
142	23.4	8.8	9	15	63	7	5	-
143	129.7	8.3	52	38	1	4	5	Silty and Sandy
151	48.2	9.2	21	7	64	8	0	Sandy and Silty
171	98.0	9.0	50	17	27	4	-	-
172	42.3	8.7	17	33	41	8	-	-

1427 These laboratory analyses results are adapted from Milewski et al. (2017).

1428